



Defence Research and
Development Canada

Recherche et développement
pour la défense Canada



Estimation of ship velocity by adaptive processing of single aperture RADARSAT-2 data

*Validation with AIS data from the Strait of
Gibraltar*

Paris W. Vachon and Marina V. Dragošević

Defence R&D Canada – Ottawa

Technical Memorandum
DRDC Ottawa TM 2009-109
August 2009

Canada

Estimation of ship velocity by adaptive processing of single aperture RADARSAT-2 data

Validation with AIS data from the Strait of Gibraltar

Paris W. Vachon
Defence R&D Canada – Ottawa
Marina V. Dragošević
TerraBytes Consulting

Defence R&D Canada – Ottawa

Technical Memorandum
DRDC Ottawa TM 2009-109
August 2009

Principal Author

Original signed by Paris W. Vachon

Paris W. Vachon
Defence Scientist

Approved by

Original signed by Caroline Wilcox

Caroline Wilcox
Head, Radar Applications & Space Technologies

Approved for release by

Original signed by Brian Eatock

Brian Eatock
Chair, Document Review Panel

© Her Majesty the Queen in Right of Canada as represented by the Minister of National Defence,
2009

© Sa Majesté la Reine (en droit du Canada), telle que représentée par le ministre de la Défense
nationale, 2009

Abstract

Adaptive processing of RADARSAT-2 synthetic aperture radar (SAR) imagery of known ships acquired near the Strait of Gibraltar provides estimates of the ship radial speed along the radar line of site and the ship aspect angle, which can be combined to provide an estimate of the ship velocity in the absence of a visible ship wake. Using a Doppler offset algorithm, it was found that the standard deviation of the radial speed estimates was 0.85 m/s for 26 ships in two HH scenes, compared to 0.3 m/s using along-track interferometry (ATI) algorithms, and was 1.3 m/s for 9 ships in a VV scene, compared to 0.6 m/s using ATI algorithms. It was shown that ship aspect angle estimation can be complicated by wave-induced ship motion, which can smear or change the orientation of the imaged ship signature. Validation was carried out against coastal-received Automatic Identification System (AIS) data. It is apparent that ship velocity estimation is feasible for single aperture SARs in the absence of a visible ship wake signature, which could be useful for tracking ships that are not transmitting AIS data.

Résumé

Le traitement adaptatif d'images de navires connus obtenues par un radar à synthèse d'ouverture (SAR) de RADARSAT-2 près du détroit de Gibraltar donne des estimations de la vitesse radiale de navires le long de l'axe de visibilité directe du radar et de l'angle d'aspect des navires, lesquelles peuvent être combinées pour obtenir une estimation de la vitesse des navires en l'absence d'un sillage visible des navires. À l'aide d'un algorithme de décalage Doppler, on a trouvé que l'écart-type des estimations de la vitesse radiale était de 0,85 m/s dans le cas de 26 navires dans deux scènes HH, par rapport à un écart-type de 0,3 m/s obtenu à l'aide d'algorithmes d'interférométrie longitudinale, et de 1,3 m/s dans le cas de 9 navires en mode VV, par rapport à 0,6 m/s obtenu avec l'algorithme d'interférométrie. On a montré qu'une estimation de l'angle d'aspect d'un navire peut être compliquée par le mouvement du navire induit par les vagues, qui peut brouiller l'image ou modifier l'orientation de la signature du navire qui paraît à l'image. Une validation a été effectuée par rapport à des données du système d'identification automatique (SIA) reçues d'une station côtière. De toute évidence, il est possible d'estimer la vitesse d'un navire pour les radars SAR à une seule ouverture en l'absence de la signature d'un sillage visible du navire, qui pourrait s'avérer utile à la poursuite des navires qui n'émettent pas de données SIA.

This page intentionally left blank.

Executive summary

Estimation of ship velocity by adaptive processing of single aperture RADARSAT-2 data

Paris W. Vachon, Marina V. Dragošević; DRDC Ottawa TM 2009-109; Defence R&D Canada – Ottawa; August 2009.

Background: Adaptive processing of synthetic aperture radar (SAR) imagery of known ships using the CHip-based Adaptive SAR Processor (CHASP) developed at DRDC Ottawa, is tested and demonstrated on three RADARSAT-2 data sets that were acquired near the Strait of Gibraltar in Moving Object Detection EXperiment (MODEX) mode. The data were acquired in this mode so that single beam range-compressed, azimuth-uncompressed Phase History Product (PHP) with sufficient fidelity could be created by using beam-forming, and so that estimated single beam ship velocities could be compared with estimates from dual-aperture SAR data. The analysis focuses on estimation of the ship radial speed along the radar line of site and the ship aspect angle. These two values can be combined to provide an estimate of the ship velocity in the absence of a visible ship wake. The radial speed is estimated by a Doppler offset algorithm that was previously developed and demonstrated for RADARSAT-1 Fine mode data. A well-calibrated physical model of the Doppler centroid (DC) serves to reduce the radial speed bias in the presence of surface currents. The ship aspect angle may be estimated from the ship signature in the image domain using several algorithms, including region growing and an Eigen-value decomposition. The ships considered were validated using coastal-received Automatic Identification System (AIS) data.

Results: The data sets include two HH and one VV acquisitions. It was found that the standard deviation of the radial speed estimates was 0.85 m/s for 26 ships in the HH scenes, compared to 0.3 m/s that was achieved using along track interferometry (ATI) algorithms on the MODEX mode data. The performance was worse for the VV scene, achieving 1.3 m/s for 9 ships, compared to 0.6 m/s achieved with ATI algorithms. A calibrated physical model for the Doppler centroid is essential for the single-beam technique to be successful.

In this work, a customized single look complex (SLC) product was generated from the MODEX mode data. The analysis shows that SLC could be a good starting point for this analysis, but a special product with a large processed bandwidth and no azimuth look weighting would be required.

Ship aspect angle estimation can be complicated by wave-induced ship motion, which will smear or change the orientation of the imaged ship signature.

Significance: Ship velocity estimation is feasible for single aperture SARs in the absence of a visible ship wake signature. From an operational perspective, this would require access to a special SLC product. Derived velocities could be used to forecast the location of ships that are not transmitting AIS data.

Sommaire

Estimation of ship velocity by adaptive processing of single aperture RADARSAT-2 data

Paris W. Vachon, Marina V. Dragošević ; DRDC Ottawa TM 2009-109 ; R & D pour la défense Canada – Ottawa ; août 2009.

Introduction : Le traitement adaptatif d'images de navires connus par un radar à synthèse d'ouverture (SAR) à l'aide du processeur SAR adaptatif à puce (CHASP), mis au point par RDDC Ottawa, a été mis à l'essai et a fait l'objet d'une démonstration faisant appel à trois jeux de données de RADARSAT-2 acquises près du détroit de Gibraltar en mode d'expérience de détection d'objets mobiles (MODEX). Les données ont été acquises dans ce mode pour qu'il soit possible de créer assez fidèlement un produit de discordance de phase (PHP) à compression de la portée d'un seul faisceau et sans compression de l'azimut, au moyen de la mise en forme des faisceaux, pour qu'il soit possible de comparer les vitesses estimées de navires à un seul faisceau à des estimations faites à partir de données de radars SAR à deux ouvertures. L'analyse porte principalement sur l'estimation de la vitesse radiale de navires le long de l'axe de visibilité directe du radar et de l'angle d'aspect des navires. Il est possible de combiner ces deux valeurs pour donner une estimation de la vitesse des navires en l'absence d'un sillage visible des navires. La vitesse radiale est estimée à l'aide d'un algorithme du décalage Doppler qui a été élaboré et a fait l'objet d'une démonstration pour les données de RADARSAT-1 en mode de résolution fine. Un modèle matériel bien étalonné du centroïde Doppler sert à la réduction de l'erreur systématique de la vitesse radiale en présence de courants de surface. L'angle d'aspect des navires peut être estimé à partir de la signature des navires dans la représentation en image à l'aide de plusieurs algorithmes, y compris la fusion de régions et une décomposition de valeurs propres. Les navires en question ont été validés à l'aide de données du système d'identification automatique (SIA) reçues d'une station côtière.

Résultats : Les jeux de données comprennent des données obtenues en deux scènes d'acquisition HH et un scène d'acquisition VV. On a trouvé que l'écart-type des estimations de la vitesse radiale était de 0,85 m/s dans le cas de 26 navires en mode HH, par rapport à un écart-type de 0,3 m/s obtenu à l'aide d'algorithmes d'interférométrie longitudinale appliqués aux données en mode MODEX. Le rendement était pire en mode VV, l'écart-type étant de 1,3 m/s dans le cas de 9 navires, par rapport à 0,6 m/s obtenu avec l'algorithme d'interférométrie. Un modèle matériel étalonné pour le centroïde Doppler est essentiel au succès de la technique faisant appel à un seul faisceau.

Dans le présent travail, un produit en format SLC (single look complex) adapté a été généré à partir des données en mode MODEX. L'analyse montre que le format SLC pourrait constituer un bon point de départ de l'analyse, mais il faudrait un produit particulier ayant une grande largeur de bande de traitement et sans pondération de l'observation de l'azimut.

L'estimation de l'angle d'aspect de navires peut être compliquée par le mouvement des navires induit par les vagues, qui brouille l'image ou modifie l'orientation de la signature des navires qui paraît à l'image.

Portée : Il est possible d'estimer la vitesse d'un navire pour les radars SAR à une seule ouverture en l'absence de la signature d'un sillage visible du navire. Du point de vue opérationnel, cela exigerait l'accès à un produit particulier en format SLC. Les vitesses dérivées pourraient servir à la prévision de l'emplacement de navires qui n'émettent pas de donnée SIA.

This page intentionally left blank.

Table of contents

Abstract	i
Résumé	i
Executive summary	iii
Sommaire	iv
Table of contents	vii
List of figures	ix
List of tables	xi
Acknowledgements	xii
1 Introduction	1
2 Properties of RADARSAT-2 SAR data collection	2
2.1 Doppler centroid model for RADARSAT-2	2
2.2 Beamforming of MODEX data	4
3 Gibraltar data sets	6
3.1 Gibraltar, 2009-01-19	7
3.2 Gibraltar, 2009-01-21	8
3.3 Gibraltar, 2009-03-10	9
3.4 Validated ships	9
4 Velocity estimation results	16
4.1 Radial speed estimation results	16
4.2 Heading estimation results	18
4.3 Experiments with SLC products	28
5 Conclusion	31
References	33

Annex A: Updated CHASP configuration	35
Annex B: Data processing procedure	45
List of acronyms	47

List of figures

Figure 1: RADARSAT-2 swaths considered overlaid on Google Map.	6
Figure 2: Land mask and relative σ^0 map for the entire Gibraltar scene from 2009-01-19.	7
Figure 3: Local calibration maps for the entire Gibraltar scene from 2009-01-19.	8
Figure 4: Local calibration maps for the entire Gibraltar scene from 2009-01-21.	9
Figure 5: Local calibration maps for the Spain sub-scene from 2009-01-21.	10
Figure 6: CDC model fitting results for the Spain sub-scene from 2009-01-21.	10
Figure 7: Residual CDC for the Atlantic sub-scene from 2009-01-21.	11
Figure 8: Residual CDC for the sub-scene off Morocco from 2009-01-21.	11
Figure 9: Residual CDC for the sub-scene off Morocco from 2009-01-21.	12
Figure 10: Land mask and relative σ^0 map for the Spain sub-scene from 2009-03-10.	12
Figure 11: Local calibration maps for the Spain sub-scene from 2009-03-10.	13
Figure 12: Local calibration maps for the Atlantic sub-scene from 2009-03-10.	13
Figure 13: Power envelope extracted by the Doppler offset algorithm.	16
Figure 14: Radial speed scatter plot for the validated ships in HH scenes.	17
Figure 15: Power envelopes extracted by the Doppler offset algorithm in the VV scene.	18
Figure 16: Radial speed scatter plot for the validated ships in the VV scene.	19
Figure 17: Aspect angle scatter plot for the validated ships on 2009-01-21.	20
Figure 18: Illustration of detected ship coordinates with the major EV orientation compared to the AIS-derived orientation.	21
Figure 19: Illustration of detected ship coordinates with the major EV orientation compared to the estimated ship location with its major EV orientation and AIS-derived orientation.	22
Figure 20: Illustration of ship imaging in a wave field with highlighted pixels detected by the DPCA algorithm and overlaid DOA-estimated positions.	23
Figure 21: Aspect angle scatter plot for the validated ships on 2009-01-19.	24

Figure 22: A short strong reflection from <i>D2S08</i> may have caused the smear in the azimuth direction.	25
Figure 23: A brief disruption in the Doppler history of <i>D1S07</i> may be due to the interference from a moving reflector on the ship, which produced the azimuth smear causing problems in aspect angle estimation.	25
Figure 24: Examples of small and fast crafts that cause problems in aspect angle estimation.	26
Figure 25: Examples of ships with good aspect angle estimates.	26
Figure 26: Aspect angle scatter plot for the validated ships on 2009-03-10.	27
Figure 27: Examples of power profiles extracted from PHP and SLC products for two ships.	29
Figure 28: Examples of accuracy degradation with reduced Doppler bandwidth.	29

List of tables

Table 1:	Data set parameters.	6
Table 2:	Ships observed on 2009-01-19.	14
Table 3:	Ships observed on 2009-01-21.	14
Table 4:	Ships observed on 2009-03-10.	15
Table 5:	Aspect angles estimated on 2009-01-21.	21
Table 6:	Aspect angles estimated on 2009-03-10.	27
Table 7:	Radial speed rmse for all ships in the SLC products with $\beta = 0$.	30
Table 8:	Radial speed rmse for all ships in the SLC products with $\beta = 2.8$.	30

Acknowledgements

We thank Dr. Charles Livingstone for his support and interest. We thank John Wolfe and Dr. Ryan English for their helpful input concerning the AIS data. We thank MDA corporation and, in particular, Dr. Anthony Luscombe, for providing the high quality RADARSAT-2 data that were used in this analysis.

1 Introduction

In earlier work, the CHip-based Adaptive SAR Processor (CHASP) [1] was used to adaptively process RADARSAT-1 data, acquired in the Fine Beam mode, and to estimate significant parameters of the detected ships [2]. Some of the estimation methods are now being tested on RADARSAT-2 data with similar properties.

This work is primarily focused on the estimation of two parameters, namely the radial speed and the ship aspect angle. Radial speed is defined as the projection of the ship's velocity onto the radar line of site (LOS). Its positive direction is away from SAR. The aspect angle is defined as the relative heading of the ship, measured in the ground plane starting from the ground projection of the LOS. Its positive direction is the same as for measuring squint, i.e., rotation about a downwards axis is taken to be positive.

Radial speed and relative heading uniquely define the velocity of the ship since the acquisition geometry is known. However, the estimation accuracy depends on many factors. In this work, radial speed is estimated by the same Doppler offset algorithm previously developed for RADARSAT-1. It has been shown that a well-calibrated physical model of the Doppler centroid (DC) plays an important role in reducing the bias of the radial speed estimates in the presence of surface currents [3]. Therefore, special attention is paid to the DC model for RADARSAT-2. The ship aspect angle is estimated by the region growing algorithm applied to the image signature, which is a very simple technique initially developed to provide rough estimates of the vessel's size and orientation. A new algorithm, based upon Eigen value decomposition of ship signature, is developed and also used in this work. Estimation errors of these algorithms are analysed in more detail than in previous work.

All SAR data used in this work have been acquired in the special split-antenna (dual channel) mode, but have been converted to single aperture (single channel) SAR data by beamforming. The main reason for this approach is that only dual channel RADARSAT-2 data are available in their raw (unfocused) form. As a result of this approach, it is also possible to compare the accuracy of the applied single-aperture adaptive algorithms to the accuracy of the well-known dual aperture techniques [4], [5].

While there is a huge body of open literature on velocity estimation with dual channel SAR, velocity estimation with single aperture SAR remains a challenging topic with very few real-world solutions.

2 Properties of RADARSAT-2 SAR data collection

The SAR data collection used in this work is similar to the RADARSAT-1 Fine Beam Mode data collection that was the basis of the previous work. The wavelength, incidence angle and resolution are all very similar. However, RADARSAT-2 has some different properties related to its steered phased-array antenna. Steering is used to create close-to-zero DC conditions for the acquired signal. Also, there is the capability of using the antenna in the split mode, which is the key feature exploited in the Moving Object Detection EXperiment (MODEX) [6]. Unfortunately, the RADARSAT-2 data policy does not make the raw signal data available for any other use, even though many applications could benefit from the Phase History Product (PHP), that is, range compressed and azimuth uncompressed. Therefore, PHP used in this work is generated by beamforming of the two-channel PHP produced in MODEX mode.

2.1 Doppler centroid model for RADARSAT-2

Under the assumption that attitude angles (yaw, ϕ_y , pitch, ϕ_p , and roll, ϕ_r) are small, a DC expression can be derived in the closed form. Linearization with respect to yaw and pitch is justified because these angles are small. In the first order approximation, roll can be absorbed into the off-nadir angle, γ . Then, a simple physical model for the stationary clutter DC (CDC) can be written in the general form:

$$f_c(\gamma) = f_{ref}(\gamma) + (\phi_y \sin(\gamma) - \phi_p \cos(\gamma))f_{for} \quad (1)$$

where f_c is the CDC and f_{ref} and f_{for} are deterministic parameters. These deterministic values can be computed as a function of the off-nadir angle and satellite state vectors (SV's), which include position (r_x , r_y and r_z) and velocity (v_x , v_y and v_z). However, SV, as well as attitude, may be expressed in any one of the several widely-used reference systems. Conventionally, SV's are given either in the Earth Centred Inertial (ECI) system or in the Earth Centred Earth Fixed (ECEF) system. Attitude is measured in a local flight system that can also be defined in various ways. The most common four reference frames are considered here. Each of them is a right-handed system with axes pointing in the forward, right and downwards directions, relative to the satellite's trajectory. The downwards direction may be defined in the geodetic sense (orthogonal to the surface of the Global Ellipsoid) or geocentric sense (pointing to the Earth center), while the forward direction can be defined with respect to the satellite's motion in the ECI or ECEF system. The most suitable choice of the flight reference system depends on the characteristics of the SAR and attitude sensors. The attitude of RADARSAT-1, which is not yaw steered, is commonly specified in the geodetic, ECI-related local system. ENVISAT is yaw steered and must maintain a geodetically horizontal position, therefore it is suitable to use the geodetic local system related to the ECEF system. RADARSAT-2 is also yaw-steered, but its reference local system is geocentric.

The following set of calculations accounts for all of these varieties:

$$\delta = \begin{cases} 0 & \text{for geocentric} \\ (R_e^2/R_p^2 - 1)(r_z - H \sin \theta_{lat}) & \text{for geodetic} \end{cases} \quad (2)$$

and

$$\omega = \begin{cases} 0 & \text{for ECEF} \\ \omega_e & \text{for ECI} \end{cases} \quad (3)$$

where R_e and R_p are the Earth Global Ellipsoid semi-major and semi-minor axes, H is the satellite altitude, θ_{lat} is the geodetic latitude and ω_e is the Earth rotation speed (assumed constant 7.2921158553e-5 rad/s). The expression for δ is valid for any of the Global Ellipsoid models, but we are using the WGS84 model. Using these values and the corresponding SV (in ECI or ECEF), further calculations are straightforward:

$$r(\delta) = \sqrt{r_x^2 + r_y^2 + (r_z + \delta)^2} \quad (4)$$

$$v_{ver}(\delta) = \frac{r_x v_x + r_y v_y + (r_z + \delta) v_z}{r(\delta)} \quad (5)$$

$$v_{hor}(\delta) = \sqrt{v_x^2 + v_y^2 + v_z^2 - v_{ver}^2(\delta)} \quad (6)$$

$$v_{for}(\delta) = v_{hor}(\delta) - \omega \frac{r_x v_y - r_y v_x}{v_{hor}(\delta)} \quad (7)$$

$$v_{down}(\delta) = -v_{ver}(\delta) \quad (8)$$

$$v_{right}(\delta) = \omega \frac{r(\delta) v_z - (r_z + \delta) v_{ver}(\delta)}{v_{hor}(\delta)} \quad (9)$$

$$(10)$$

For a SAR operating at wavelength λ (the carrier wavelength), the reference values in (1) are:

$$f_{ref}(\gamma) = \frac{2}{\lambda} (v_{down}(\delta) \cos \gamma + v_{right}(\delta) \sin \gamma) \quad (11)$$

$$f_{for} = -\frac{2}{\lambda} v_{for}(\delta) \quad (12)$$

At the level of first order approximation, CDC depends linearly on yaw and pitch and can be calculated easily for a given off-nadir angle, i.e., for all slant range bins.

If we choose the geocentric, ECEF related reference frame for attitude, RADARSAT-2's yaw-steering is included in f_{ref} , while the attitude ϕ_y and ϕ_p in (1) represents the residual offset between the actual pointing and the reference (nominal) pointing based on the yaw-steering law. For this reason, the offset can be considered constant over a period of slow time. In particular, if ϕ_y and ϕ_p are estimated from the SAR signal at some place along the orbit that has suitable clutter properties, they may also be used at a near-by place where the stationary CDC cannot be extracted from the SAR signal directly. This approach is used to establish stationary CDC values over the patches of water using the measurements taken over the land within the same SAR scene.

Unlike RADARSAT-1, RADARSAT-2 auxiliary data provide an on-board measurement of the attitude angles with reasonable accuracy. According to RADARSAT-2 documentation [7], the auxiliary attitude values are in the geocentric, ECI related reference frame. They are variable over slow time because yaw steering is time variant in this reference frame. The auxiliary attitude values are recorded (8 per second) and can be used in the CDC calculations if direct CDC estimation is not possible. This is an alternative approach which may be used when the scene is entirely over ocean.

2.2 Beamforming of MODEX data

MODEX-1 mode is an experimental dual-channel mode designed for MODEX, where the pulses are transmitted by the full antenna and received in parallel by the two wings of the antenna, usually referred to as fore and aft. This configuration can be used for:

- Displaced Phase Center Antenna (DPCA) technique for moving target detection;
- Along track interferometry (ATI) technique for estimation of target radial speed;
- Direction of Arrival (DOA) technique for estimating the azimuth position of the target.

Apart from these typical dual-channel applications, the fore and aft signals can also be coherently combined to produce the equivalent of the full antenna receive signal. Beamforming is a linear coherent operation that can steer the beam to attain a maximum (or to create a notch) in the desired direction (or directions when the number of channels is more than two). In our case, it is desirable to restore the beam pattern of the original, full length antenna by a linear combination:

$$\mathbf{S} = [\mathbf{S}_{fore} \mathbf{S}_{aft}] \mathbf{G} \quad (13)$$

where \mathbf{G} is the so-called steering vector. Assuming that beams of both wings point in the same direction and assuming that the beam patterns are identical (in magnitude and phase), this would be achieved by simply adding the fore and aft signals, i.e., $\mathbf{G}^H = [1 1]$. However, the fore and aft channels have a slight gain imbalance and a phase offset, which needs to be corrected before summing them together. Yet another problem is the slight pointing difference for the two antenna beams, which is evident from Doppler centroid estimates performed on each channel separately. This problem could be mitigated by a range-dependent \mathbf{G} , but the range-dependent effect is judged to be small and is ignored in this work. It is expected that a better alignment of the fore and aft beams will be achieved in the near future by implementing a suitable weighting across the antenna columns. This correction has already been up-loaded and tested for some modes, but has not been applied to the beams used in this analysis. Therefore, there is a small loss of coherence in our data sets.

The beamforming operation can be done after the front-end processing and subsequent linear operations in the SAR processor. In this case, it was performed on the PHP after range compression.

For the Gibraltar data sets considered here, the form of the steering vector is:

$$\mathbf{G} = \begin{bmatrix} 1 \\ g_c \exp(j\phi_c) \end{bmatrix} \quad (14)$$

and the optimum gain achieved is slightly over 5 dB (compared to the fore channel alone). Under ideal conditions, it would be 6 dB. This gain is measured by comparing the estimated relative σ^0 for some selected land area over Spain and Morocco. Alternative steering, such as broadside (which would create zero Doppler conditions), has also been considered, but this provided a lower gain. At the same time, the noise level increased by 3 dB compared to a single channel acquisition since noise is summed incoherently and $g_c \approx 1$. Therefore, the signal-to-noise ratio (SNR) is worse than in the regular single-channel acquisition, but the signal-to-clutter ratio (SCR) is preserved. The beam

width corresponding to \mathbf{S}_{fore} and \mathbf{S}_{aft} is reduced in \mathbf{S} to the value expected for the full antenna and the coherent integration time is reduced accordingly.

The power imbalance compensation, g_c is easy to measure. The phase imbalance compensation, ϕ_c can be found by searching for the largest attainable beamforming gain. However, a more direct method was used. Based on many data sets, it has been found that the average ATI phase offset, ϕ_{cal} , and the CDC satisfy:

$$\phi_{cal} = -2\pi \frac{d}{v_s} f_c - \phi_c \quad (15)$$

where d is the effective baseline and v_s is the satellite speed. Proportionality between the average ATI offset and CDC is expected because both depend on the antenna squint. The constant term, ϕ_c describes an electronic offset between the channels. Based on fitting over different scenes, its value is found to be 0.331 for HH polarization and -2.319 for VV polarization.

3 Gibraltar data sets

The data sets used in this report were acquired over Gibraltar in the MODEX-1 mode, with properties summarized in Table 1 and swaths shown in Fig. 1. The third pass is the same as the second, but taken with a different polarization 48 days later. All data sets have the same pulse duration of $41.6\mu\text{s}$ and the same pulse bandwidth (BW) of 30 MHz, which are almost identical to the pulse parameters of the RADARSAT-1 Fine Beam mode. The pulse repetition frequency (PRF) is somewhat higher to match the higher Doppler bandwidth of the MODEX signal.

Table 1: Data set parameters.

data set	date yyyy-mm-dd	pass	off-nadir angle [°]	pulse BW [MHz]	pulse polarization	PRF [Hz]
<i>D1</i>	2009-01-19	ascending	44.30	30	HH	1802.09
<i>D2</i>	2009-01-21	descending	37.10	30	HH	1825.15
<i>D3</i>	2009-03-10	descending	37.10	30	VV	1825.15

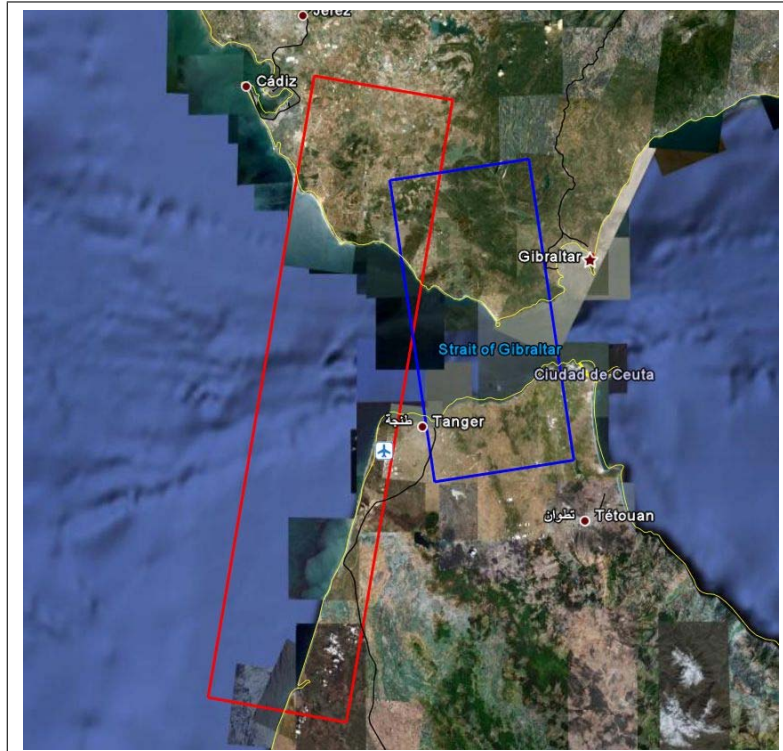


Figure 1: RADARSAT-2 swaths considered overlaid on Google Map (©2009 Google - Map data ©2009 Europa Technologies).

3.1 Gibraltar, 2009-01-19

A map of the local CDC was produced by running CHASP on small image chips from throughout the entire data set. This scene is about 75 km long. A land mask was used to select image chips belonging to land. After CDC fitting over land, the attitude angles were estimated to be 0.0204° yaw and 0.0192° pitch, which is within RADARSAT-2 specifications [8]. In Fig. 2, it is clear that the land chips correspond to much higher σ° , although the data are not absolutely calibrated. This figure also shows the uniformity of the scene, which is important for good DC estimation. In the maps shown in Fig. 3, there is a clear difference between the land and sea surface. The surface currents have a positive radial speed, i.e., away from the SAR, which means West to East for this ascending, right-looking, scene. There appears to be an anomaly in the CDC maps close to the coastlines. There is a reasonable explanation for this artifact. It may be attributed to the sidelobes coming from the land and contributing to the estimated CDC in the areas of low ocean back scatter, which is a consequence of the HH polarization, high incidence angle and relatively calm sea surface.

As a consistency check, the CDC map was compared to the dual channel calibration map, estimated by adaptively balancing the fore and aft channels, and also by running CHASP on small data chips. Dual channel balancing is based on the requirement that the ATI phase should be zero for the stationary clutter. This is achieved by estimating and removing the phase offset, which may be present between the co-registered complex images from the two channels. This phase offset, ϕ_{cal} , may be spatially variable, just like CDC. It has been found that the two maps are highly correlated (proportional, but with opposite signs). This is expected since both CDC and the channel phase imbalance depend on the antenna squint. This is an important feature for our analysis because the beamforming approach depends on it. Moreover, the same artifact occurs along the shore for both methods.

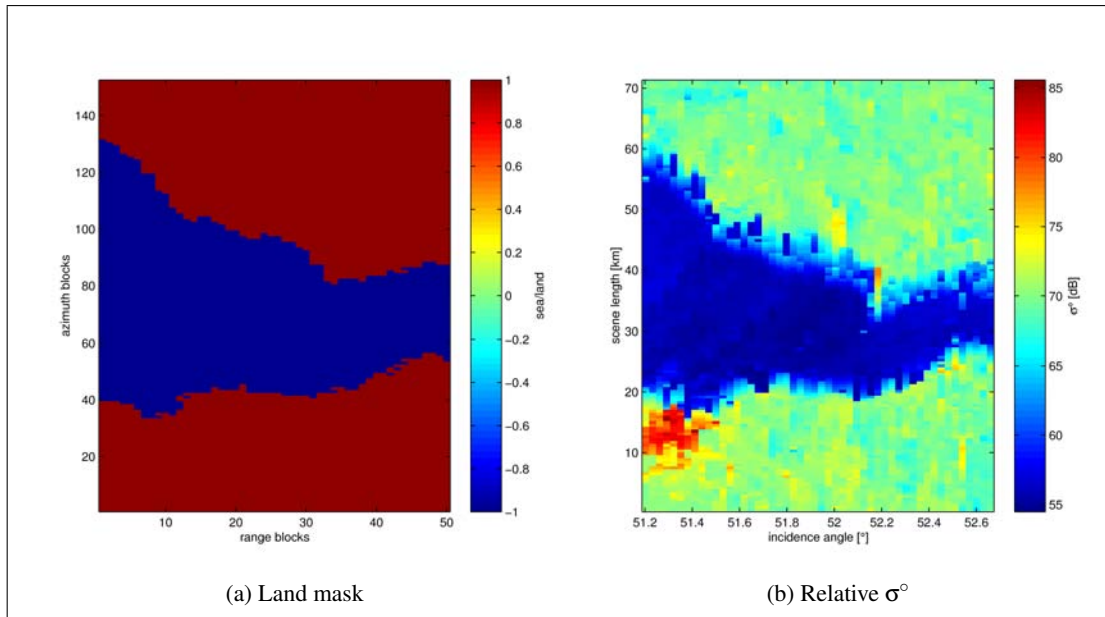


Figure 2: Land mask and relative σ° map for the entire Gibraltar scene from 2009-01-19.

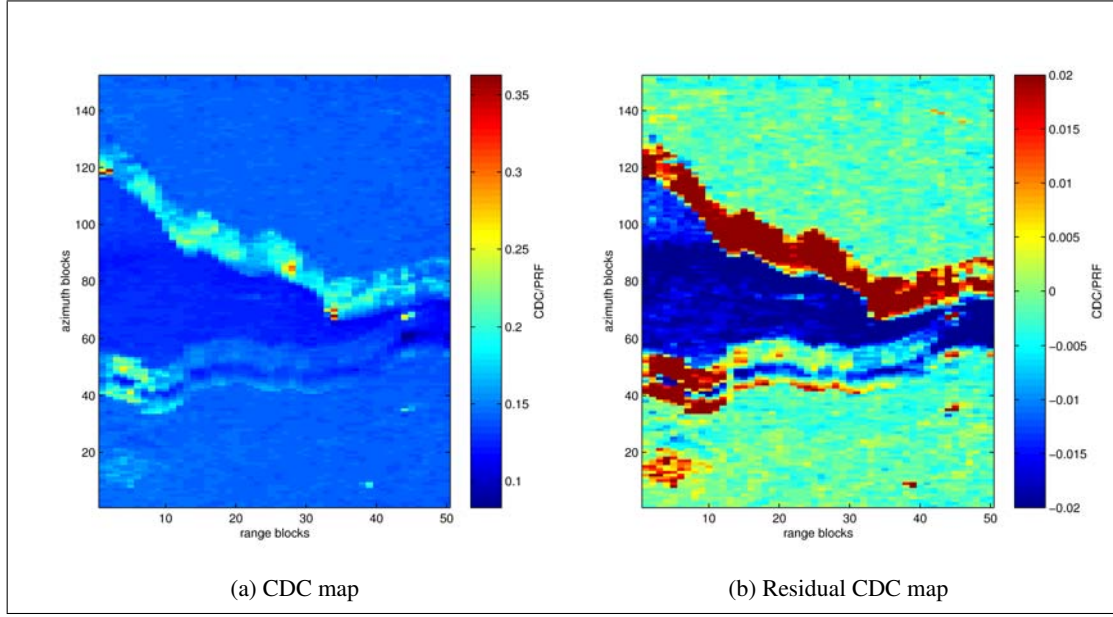


Figure 3: Local calibration maps for the entire Gibraltar scene from 2009-01-19.

3.2 Gibraltar, 2009-01-21

This scene is around 155 km long and includes more water than land. For the entire scene, the CDC map is compared to the ϕ_{cal} map as shown in Fig. 4. Both maps were produced by CHASP within identical image chips. As expected, these maps are correlated. Outliers appear in both maps and can be associated with the local intensity contrast and motion. There is also a clear difference between the land and sea surface. The surface currents have a negative radial speed, i.e., towards the SAR, which, again, means West to East for this descending, right-looking, scene. Certain areas in this scene have very large CDC deviations compared to the calibrated physical model. Surface motion in such areas, if uncompensated, may contribute up to 0.7 m/s to the radial speed estimates. Other areas in the same scene are less affected. There are no noise-dominated regions in this scene. For this long scene, processing was done in three separate sub-scenes and more refined CDC estimates were produced for each. The first sub-scene is over Spain and served for CDC calibration. The results of local CDC estimation are presented in the Fig. 5 for the beamformed signal and compared to the predicted DC values, derived for the RADARSAT-2 nominal steering law. In this case, smaller image tiles are used to produce a finer map than in Fig. 4 and median filtering was applied within each tile to minimize the effects of local discontinuities in the backscatter reflectivity. After fitting, the attitude angles are estimated to be 0.0238° yaw and 0.0255° pitch, which is within RADARSAT-2 specifications and, in fact, very close to the estimates from the 2009-01-19 scene. Estimates for separate channels were somewhat different, as discussed earlier (0.0464° fore yaw, 0.0403° fore pitch, 0.0040° aft yaw, 0.0221° aft pitch). The fitting error is shown in Fig. 6. The applied CDC estimation algorithm works best for uniform scenes. The relative σ° map is included for reference.

The calibrated model was then applied to the other two sub-scenes with ocean and ships. As discussed earlier, this approach relies on the assumption that the attitude remains the same in the

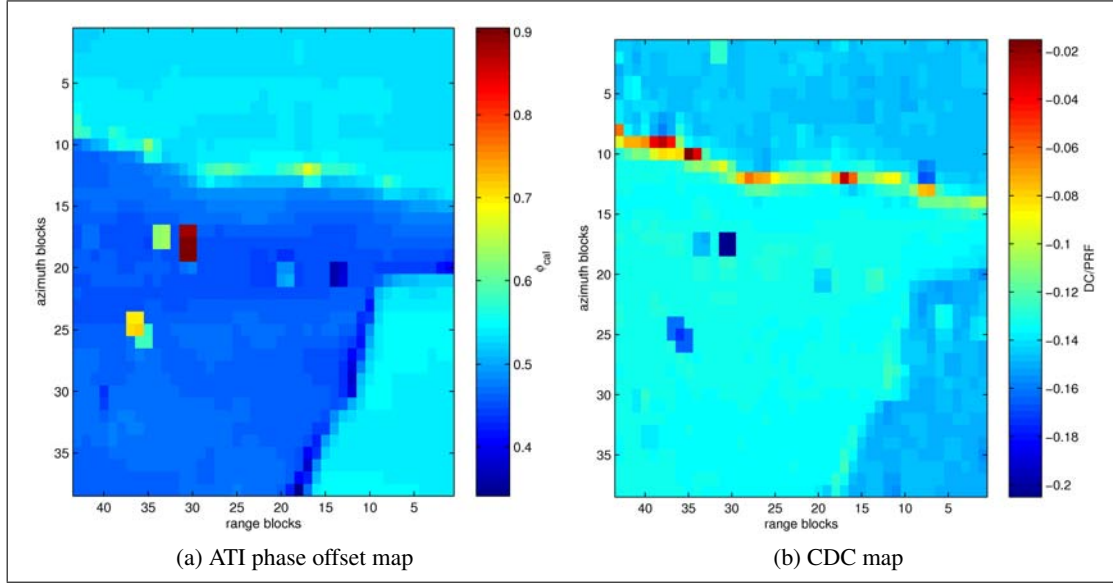


Figure 4: Local calibration maps for the entire Gibraltar scene from 2009-01-21.

adopted reference frame. In other words, the change due to yaw-steering is accounted for, but the deviation from it is assumed to be constant. This assumption is now confirmed. Fig. 7 shows the difference between the calibrated model (from Spain) and the measured CDC for the second sub-scene, which is over the Atlantic ocean, with no land. The third sub-scene is over the Atlantic with the Morocco coast at near range. The land mask and the relative σ^0 map are shown in Fig. 8 and the residual CDC is shown in Fig. 9. The reference attitude for this sub-scene is still from the Spain sub-scene, but does match the CDC well over the land of Morocco.

3.3 Gibraltar, 2009-03-10

This is a repeat pass, but with a different polarization. The data were acquired 48 days (two repeat pass cycles) after the 2009-01-21 data. CDC was calibrated in the same way, using only the patch of data over Spain. The calibration maps are shown in Fig. 10 and 11. From these maps, the estimated attitude for this scene is 0.0308° yaw and 0.0236° pitch. All ships appear in a sub-scene over the Atlantic. The σ^0 and CDC maps for the Atlantic sub-scene are shown in Fig. 12. These maps are less uniform than the corresponding maps from 2009-01-21.

3.4 Validated ships

There are 17 AIS-validated moving ships in the 2009-01-19 data set, as listed in Table 2. There are 9 AIS-validated moving ships in the 2009-01-21 data set, as listed in Table 3. There are 9 AIS-validated moving ships in the 2009-03-10 data set, as listed in Table 4. Their length, L , speed, V and heading, θ were extracted from the AIS data. The radial speed, V_T , can be derived using the imaging geometry. The incidence angle, α_{inc} , is also derived from the geometry.

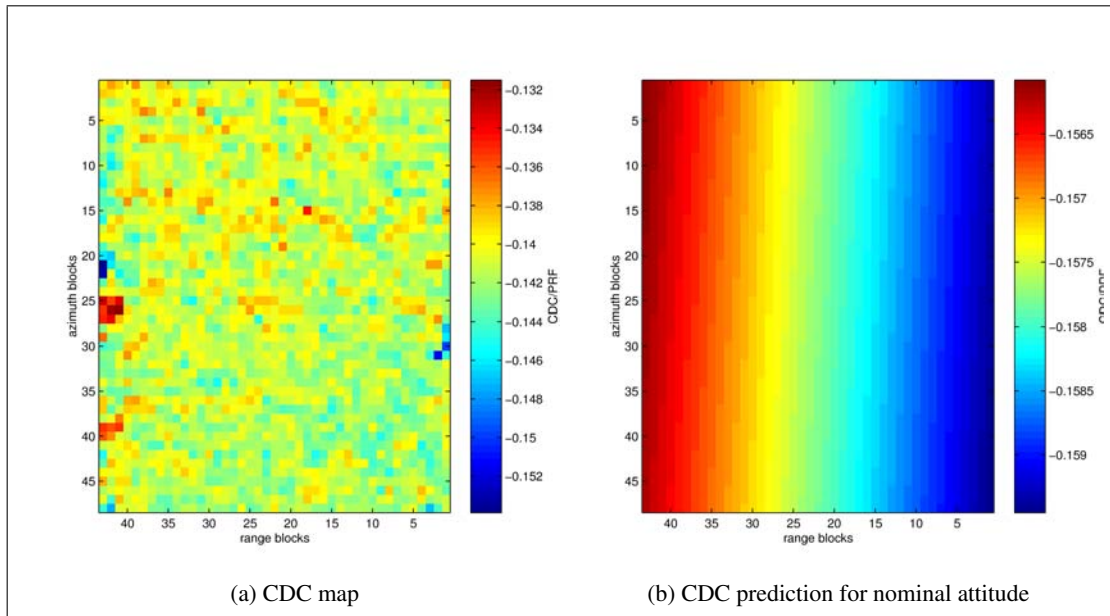


Figure 5: Local calibration maps for the Spain sub-scene from 2009-01-21.

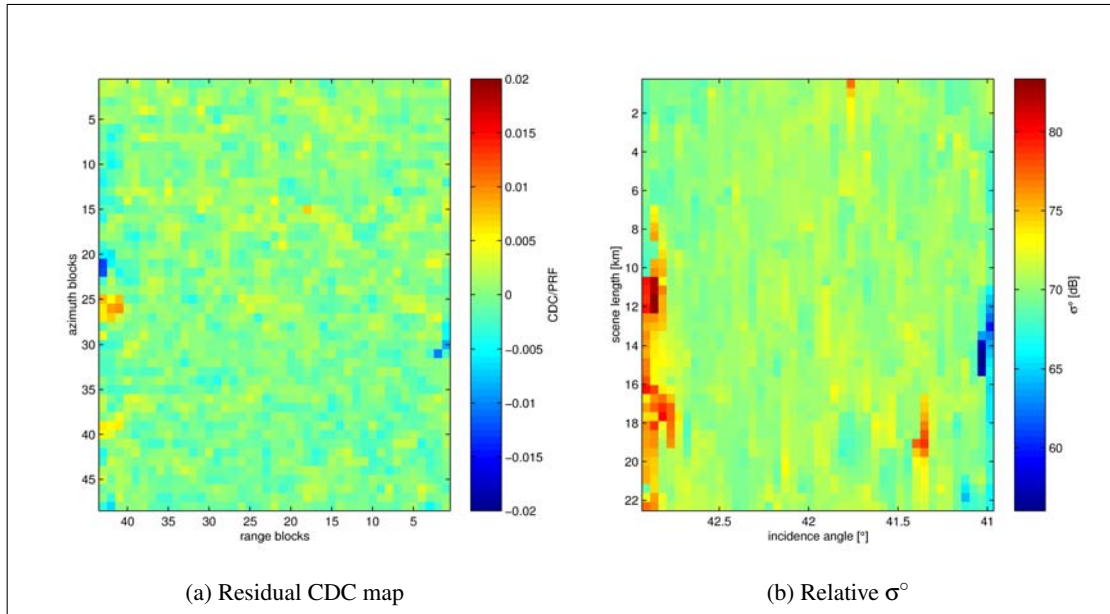


Figure 6: CDC model fitting results for the Spain sub-scene from 2009-01-21.

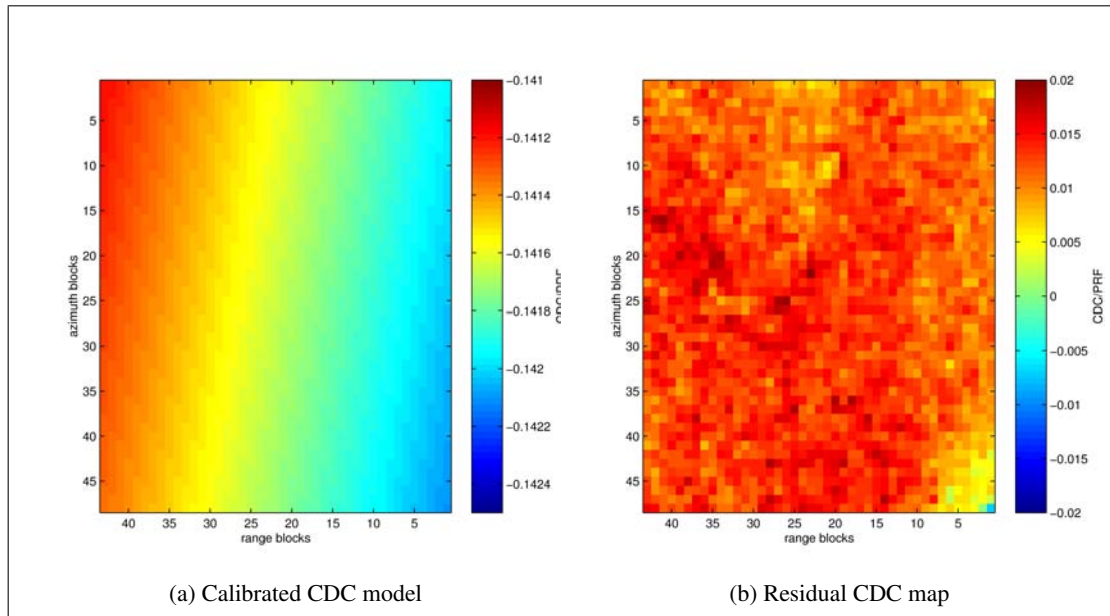


Figure 7: Residual CDC for the Atlantic sub-scene from 2009-01-21.

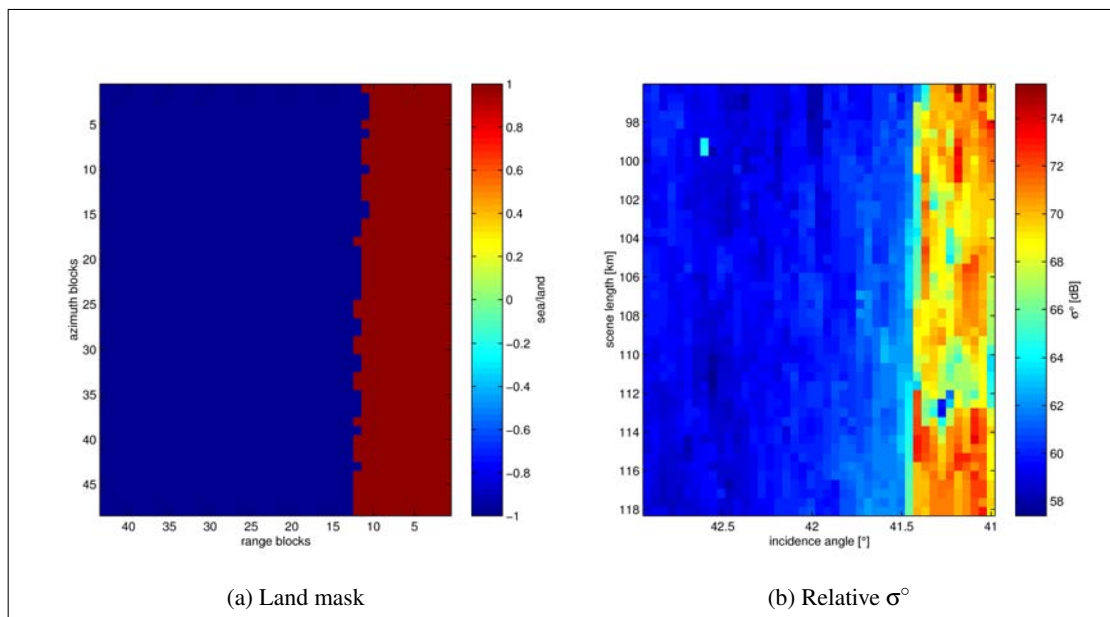


Figure 8: Residual CDC for the sub-scene off Morocco from 2009-01-21.

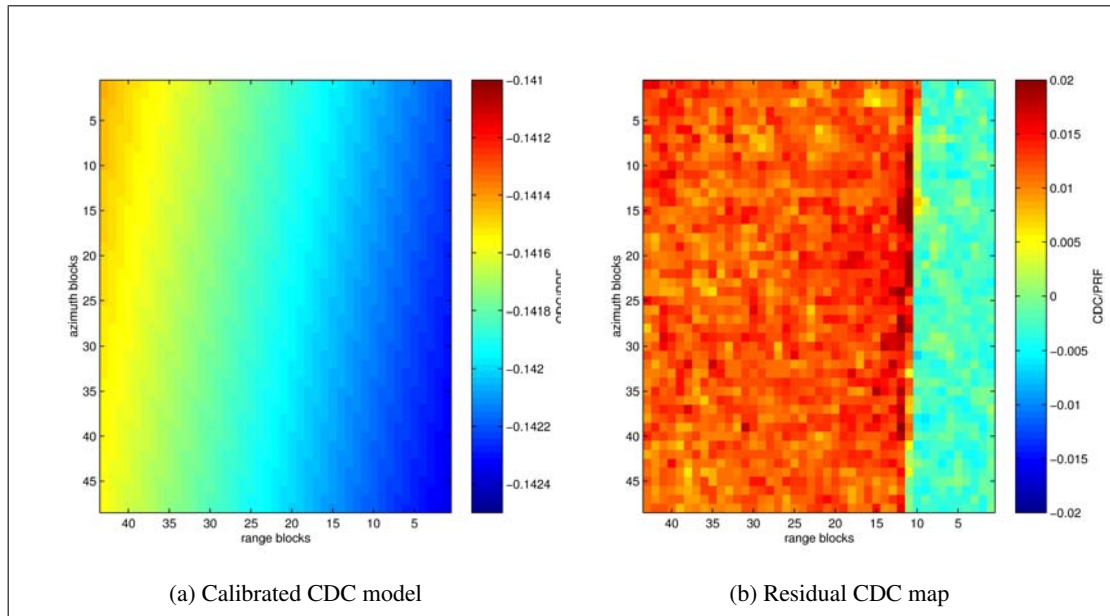


Figure 9: Residual CDC for the sub-scene off Morocco from 2009-01-21.

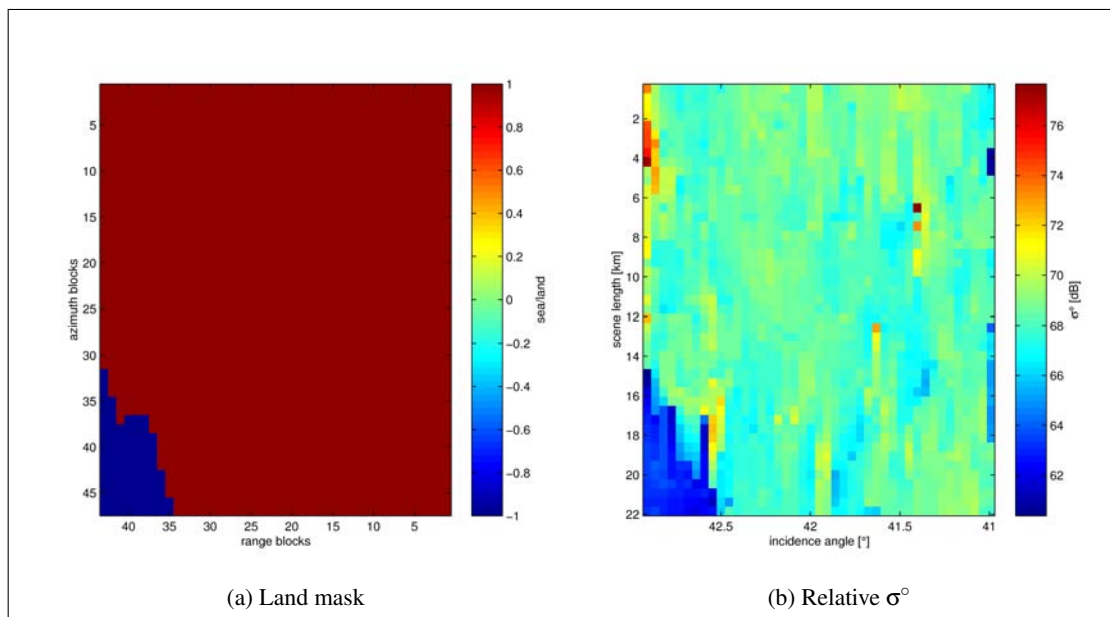


Figure 10: Land mask and relative $\tilde{\sigma}^\circ$ map for the Spain sub-scene from 2009-03-10.

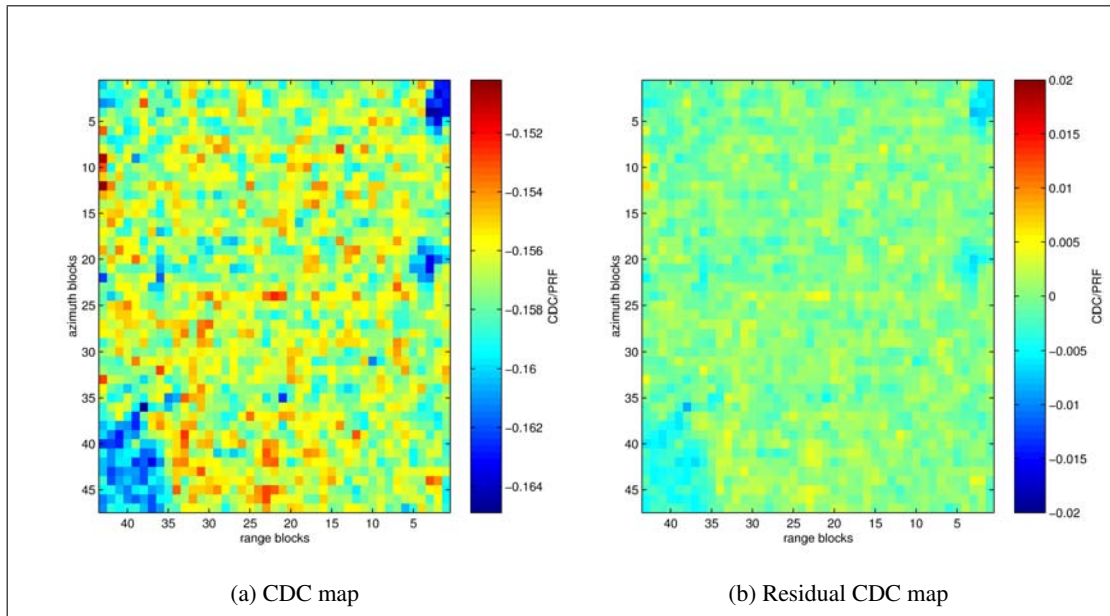


Figure 11: Local calibration maps for the Spain sub-scene from 2009-03-10.

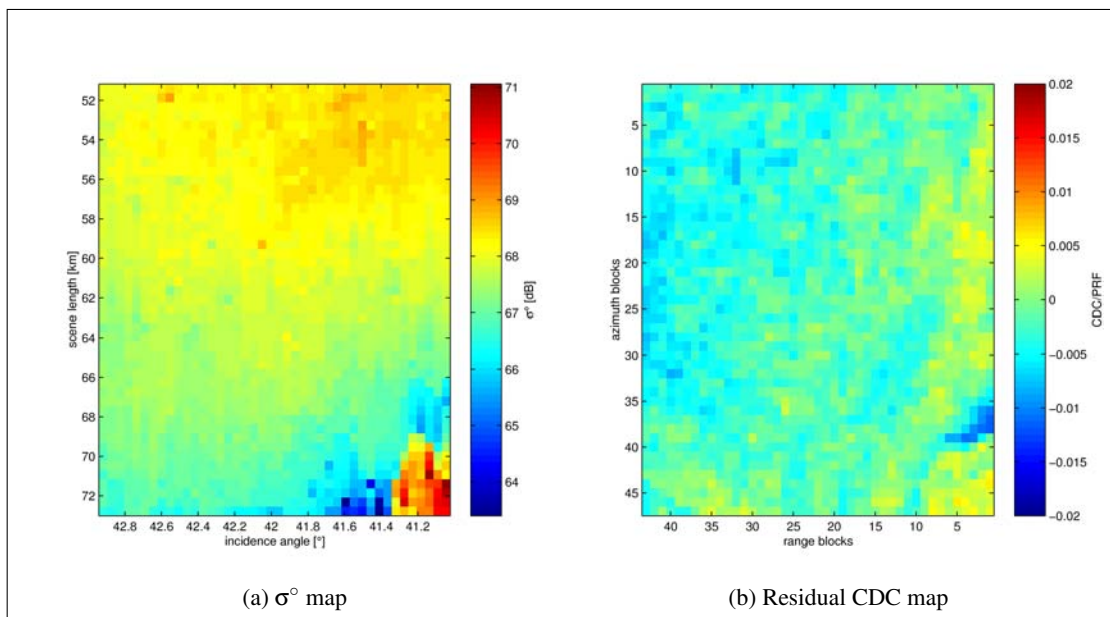


Figure 12: Local calibration maps for the Atlantic sub-scene from 2009-03-10.

Table 2: Ships observed on 2009-01-19.

ship	AIS			derived	
	L [m]	V [m/s]	θ [$^{\circ}$ T]	V_T [m/s]	α_{inc} [$^{\circ}$]
<i>DIS01</i>	86	18.09	45.9	11.559	51.7
<i>DIS02</i>	333	6.06	252.9	-4.744	52.3
<i>DIS03</i>	172	6.43	252.7	-5.037	52.4
<i>DIS04</i>	101	5.14	84.4	4.050	52.1
<i>DIS05</i>	99	7.58	76.1	5.911	51.5
<i>DIS06</i>	193	6.38	270.0	-4.961	51.9
<i>DIS07</i>	122	6.93	258.4	-5.452	52.0
<i>DIS08</i>	115	9.44	67.3	7.203	51.9
<i>DIS09</i>	87	14.87	246.8	-11.332	52.0
<i>DIS10</i>	181	8.75	271.9	-6.708	51.2
<i>DIS11</i>	115	6.71	89.0	5.212	51.6
<i>DIS12</i>	88	3.64	250.5	-2.819	52.2
<i>DIS13</i>	215	7.48	252.0	-5.856	52.6
<i>DIS14</i>	142	7.56	267.0	-5.885	51.9
<i>DIS15</i>	250	6.45	247.0	-4.934	52.1
<i>DIS16</i>	132	4.94	252.2	-3.871	52.5
<i>DIS17</i>	125	5.30	251.6	-4.139	52.5

Table 3: Ships observed on 2009-01-21.

ship	AIS			derived	
	L [m]	V [m/s]	θ [$^{\circ}$ T]	V_T [m/s]	α_{inc} [$^{\circ}$]
<i>D2S01</i>	147	7.55	212.6	1.976	42.6
<i>D2S02</i>	196	9.92	265.9	6.489	42.4
<i>D2S03</i>	123	5.66	229.2	2.389	41.9
<i>D2S04</i>	225	5.33	272.1	3.566	42.5
<i>D2S05</i>	69	5.15	89.5	-3.382	41.9
<i>D2S06</i>	200	8.41	225.7	3.338	42.6
<i>D2S07</i>	176	7.67	32.7	-2.024	42.8
<i>D2S08</i>	108	4.67	282.0	3.148	42.8
<i>D2S09</i>	157	7.13	71.2	-4.148	41.6

Table 4: Ships observed on 2009-03-10.

ship	AIS			derived	
	L [m]	V [m/s]	θ [$^{\circ}$ T]	V_T [m/s]	α_{inc} [$^{\circ}$]
<i>D3S01</i>	128	7.77	271.1	5.068	41.3
<i>D3S02</i>	274	7.60	89.3	-5.078	42.8
<i>D3S03</i>	117	4.97	89.4	-3.244	41.6
<i>D3S04</i>	115	6.10	271.3	4.004	41.6
<i>D3S05</i>	205	6.51	52.7	-2.973	42.2
<i>D3S06</i>	190	7.88	93.4	-5.315	42.7
<i>D3S07</i>	225	6.99	271.7	4.589	41.5
<i>D3S08</i>	179	6.43	90.8	-4.266	42.2
<i>D3S09</i>	132	6.61	90.5	-4.290	41.2

4 Velocity estimation results

Velocity estimation includes radial speed estimation and heading estimation. Radial speed estimation is based on the Doppler offset. Heading estimation is based on estimation of the aspect angle of the ship in the image domain.

4.1 Radial speed estimation results

Radial speed estimation is done on the beamformed PHP using the same Doppler offset algorithm and software as was used in the case of RADARSAT-1 data [2]. The only difference is that local CDC estimation was disabled while processing ships. A new utility was developed to provide CDC values according to the calibrated model, which were fed into CHASP as external settings. With this approach, no additional corrections are needed.

The effect of beamforming is seen in Fig. 13 where power profiles of the fore, aft and beamformed signal are compared at the output of the adaptive filter used for SCR and SNR enhancement [3]. This figure illustrates that the ship signature is extracted well from the background when adaptive filtering is applied to each of the channels separately and, also, when applied to the beamformed signal in slow time. The sharper slope at the leading and trailing end of the ship's power profile, after beamforming, makes it easier to estimate the acquisition time (beam centre time) at which the Doppler offset must be estimated. Results for 2009-01-19 and 2009-01-21 are summarized in the

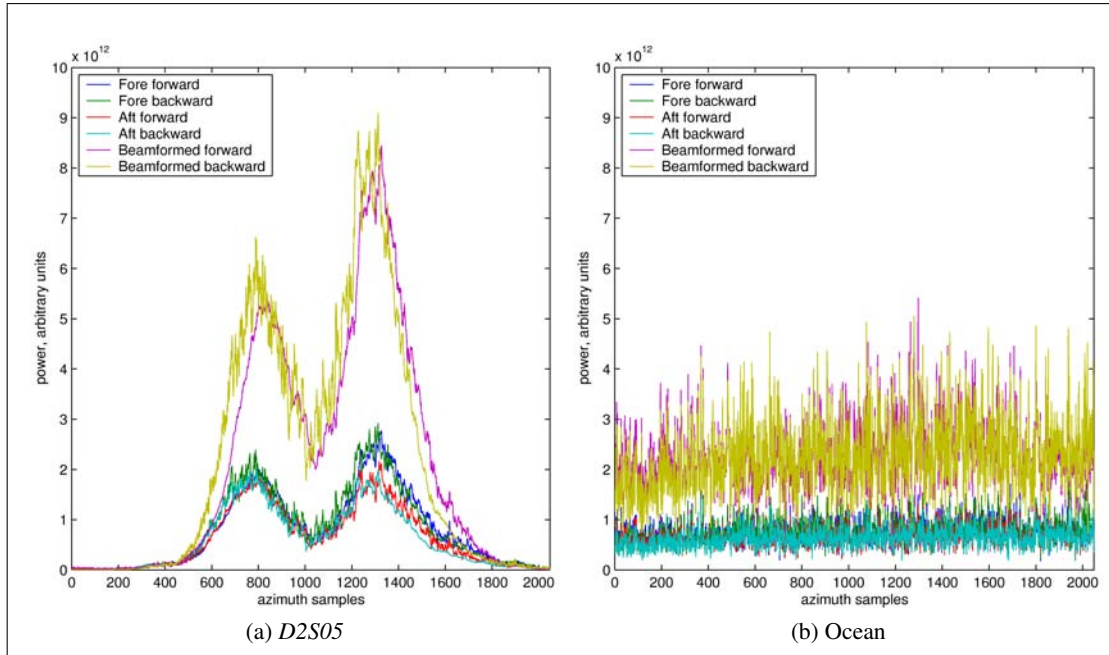


Figure 13: Power envelope extracted by the Doppler offset algorithm.

scatter plot in Fig. 14. The over-all standard deviation of the radial speed estimates is 0.85 m/s, which is almost the same as the accuracy of the RADARSAT-1 estimates obtained from the Fine

Beam scenes over the Strait of Dover. For comparison, the standard deviation of the radial speed estimates based on the dual-channel ATI method is 0.3 m/s. The ATI method achieves higher accuracy at the expense of additional receiver hardware and, typically, a reduced swath. Both methods face the same problem in the presence of surface motion since they both require calibration. Both methods gave better results for the 2009-01-19 scene than the 2009-01-21 scene. In the latter scene, the incidence angle was smaller and SCR was lower. It is also possible that the weather conditions contributed to the difference noted between these two scenes. Radial speed estimation

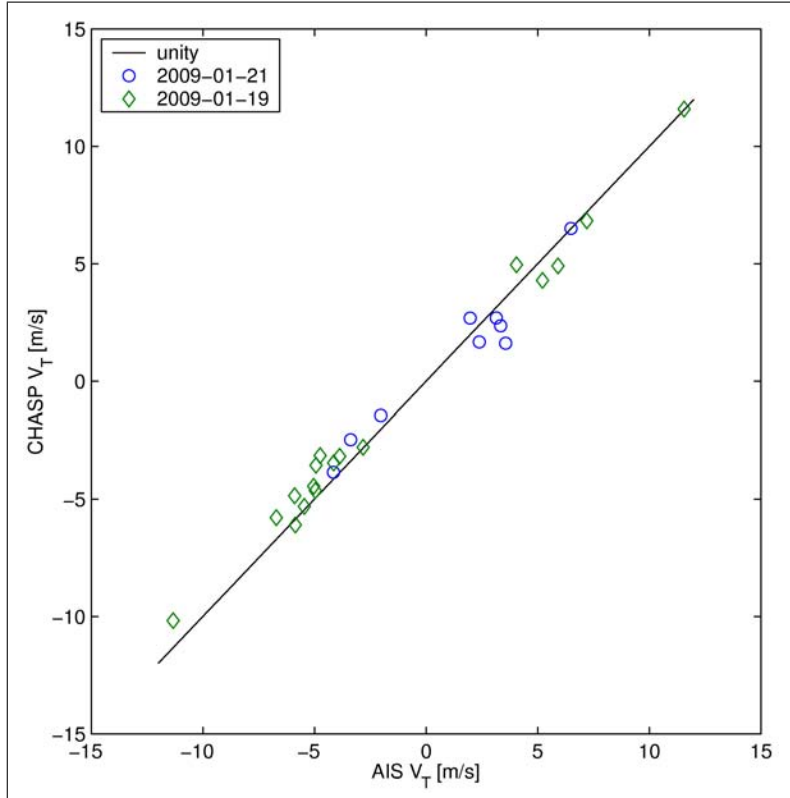


Figure 14: Radial speed scatter plot for the validated ships in HH scenes.

was more difficult in the VV scene from 2009-03-10. In this case, the adaptive algorithm for Doppler tracking was faced with a lower SCR, which is evident in Fig. 15. As a result, there was a larger estimation error. As demonstrated in Fig. 16, the speed estimates are biased towards zero. An explanation for this bias lies in the nonstationary character of the clutter upon deramping so that tracking initiates under different clutter conditions depending on the Doppler offset of the tracked ship and depending on the starting position in slow time. Due to this effect, there is an unequal latency of the forward and backward tracking, as seen in Fig. 15. For a ship with negative radial speed (positive Doppler offset), forward tracking commences slower than backward tracking (case (a) in Fig. 15). For a ship with positive radial speed (negative Doppler offset), backward tracking commences slower than forward tracking (case (b) in Fig. 15). Being non-symmetrical, tracking delays do not fully compensate each other, giving rise to a bias in the estimate of the signature acquisition time, which affects the estimation of the Doppler offset. The same effect is

also noticeable in Fig. 13 for HH data, but to a smaller degree. In principle, the algorithm could be improved. However, possible improvements are not considered in this report. Standard deviation of the estimation error was roughly 50% larger than for the 2009-01-21 HH scene (acquired in the same mode over the same region). For the dual-channel ATI method, standard deviation of the VV estimates was approximately doubled when compared to the standard deviation of the HH estimates from 2009-01-21.

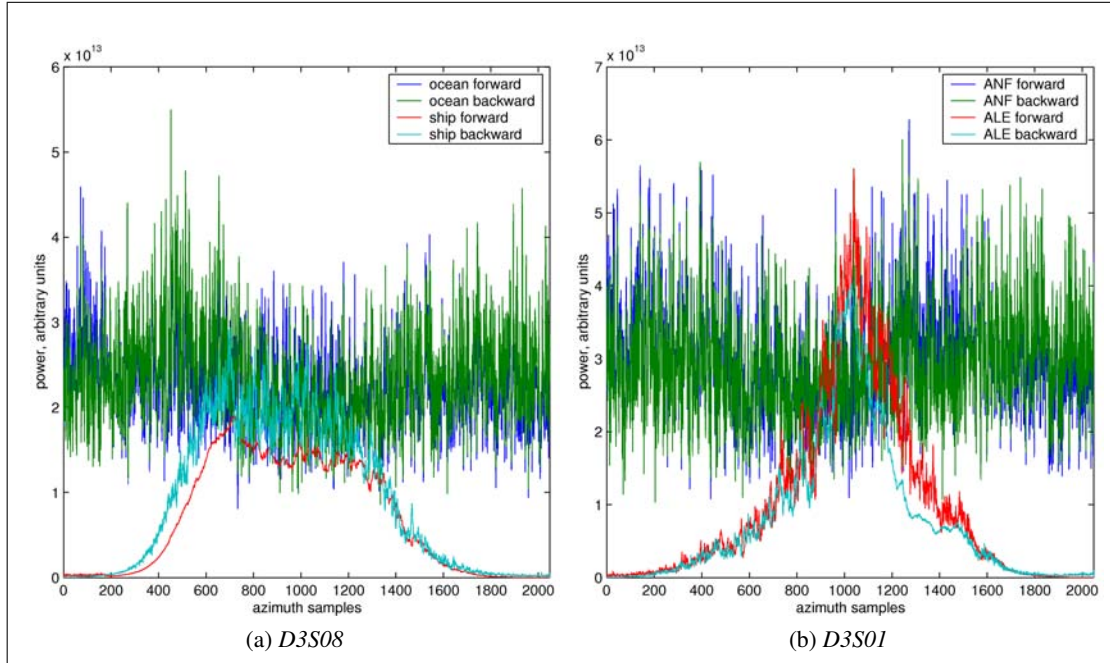


Figure 15: Power envelopes extracted by the Doppler offset algorithm in the VV scene.

4.2 Heading estimation results

Relative heading, also referred to as the aspect angle, can be estimated in the image domain.

The estimation algorithm based on region growing that was used for RADARSAT-1 data [2] was applied in this case. Compared to the RADARSAT-1 data that were collected in the Strait of Dover, there were more estimation problems in the RADARSAT-2 Gibraltar data sets. Different problems occurred for different scenes. Therefore, the results from the three scenes are presented separately.

For example, the results for 2009-01-21 are summarized in the scatter plot in Fig. 17 and in the Table 5. Out of nine ships in this scene, there are two obvious outliers, *D2S01* and *D2S07* and yet another ship, *D2S08*, has a large error. This problem was explored further using two other approaches to estimate the orientation of the ships. Several interesting cases were studied to understand better the origin of the problems.

The revised algorithm for estimating the aspect angle starts from the list of detected ship pixels.

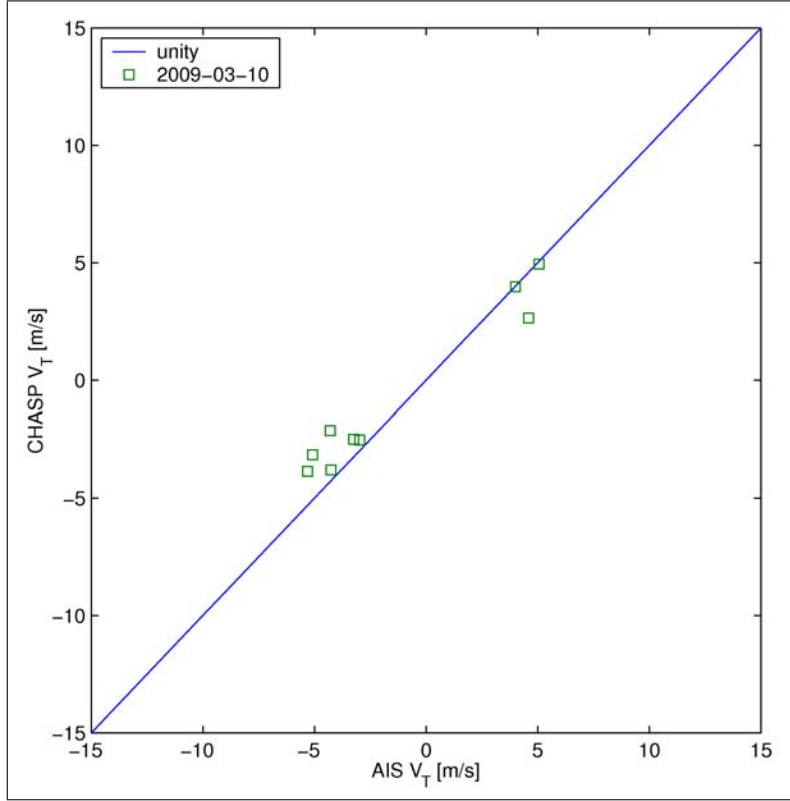


Figure 16: Radial speed scatter plot for the validated ships in the VV scene.

Assuming that (x_k, y_k) , $k \in (1, 2, \dots, n)$, represents the image coordinates of a detected pixel scaled to the units of length on the ground (meters), the matrix of the detection coordinates, \mathbf{D} can be formed as follows:

$$\mathbf{D} = \begin{bmatrix} x_1 & y_1 \\ x_2 & y_2 \\ \vdots & \vdots \\ x_n & y_n \end{bmatrix} \quad (16)$$

and translated to the centre of gravity:

$$\mathbf{D}_c = \left(\mathbf{I} - \frac{1}{n} \begin{bmatrix} 1 & \dots & 1 \\ \vdots & & \vdots \\ 1 & \dots & 1 \end{bmatrix} \right) \mathbf{D} \quad (17)$$

Ships are usually elongated in one direction, so that the Hermitian matrix

$$\mathbf{R} = \mathbf{D}_c^T \mathbf{D}_c \in \mathbb{R}^2 \quad (18)$$

tends to have unequal eigenvalues, λ_{max} and λ_{min} . In this case, the major eigenvector \mathbf{V}_{max} (corresponding to λ_{max}) indicates the dominant orientation, while the minor eigenvector \mathbf{V}_{min} is its

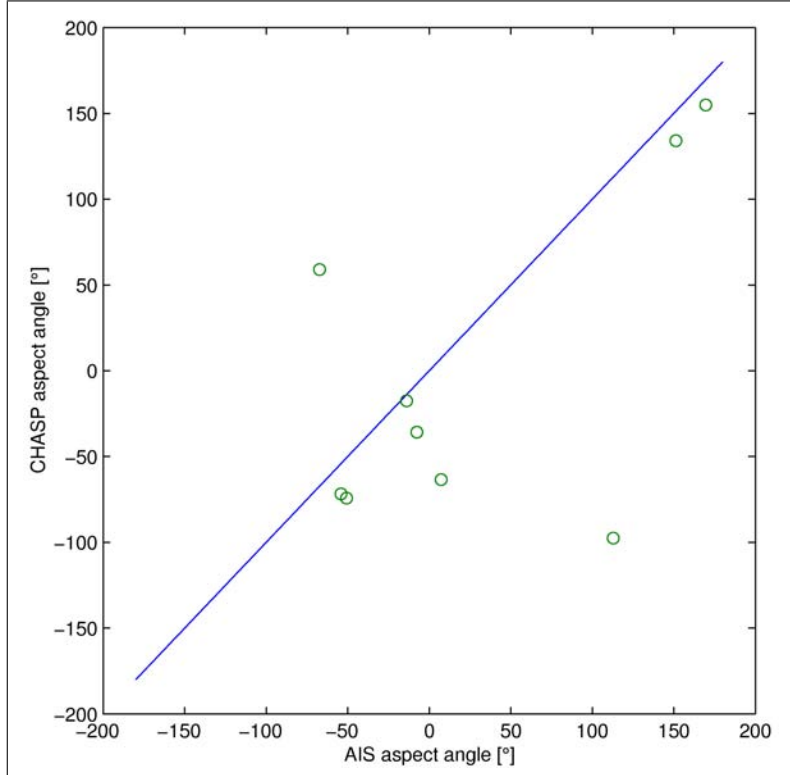


Figure 17: Aspect angle scatter plot for the validated ships on 2009-01-21.

orthogonal complement. In other words, the rotation

$$\mathbf{Q} = [\mathbf{V}_{max} \mathbf{V}_{min}] \quad (19)$$

reveals the major and minor axes of the vessel. To improve accuracy, points in \mathbf{D} are weighted by their corresponding magnitudes before performing the eigenvalue (EV) decomposition. An illustration of this simple concept is shown in the example of two ships from the 2009-01-21 data set in Fig. 18. In both cases, the EV-based orientation is visually acceptable, but is not collinear with the AIS-derived orientation. In most cases, the EV-based estimates agree well with the estimates from the region growing algorithm, as presented in Table 5.

The discrepancy between our estimates and the AIS data may be explained by the effects described and analysed by Ouchi et al. [9]. In the wave regime, ships exhibit rotation so that their linear speed varies along the ship (from the bow to the stern) and, possibly, with height. Thus, rotational motion can cause a different azimuth shift for different portions of the ship, which produces a distortion in the image.

To further investigate this assumption, the dual-channel aspect of the SAR data was used. The two wings of the antenna form a two element array that can be used to reveal the direction of arrival. A very simple DOA algorithm [10] was applied to all pixels to estimate their position in azimuth. This algorithm is not sensitive to the radial speed and should not be affected by ship motion. For

Table 5: Aspect angles estimated on 2009-01-21.

ship	AIS [°]	algorithm		
		region growing [°]	EV detected [°]	EV located [°]
<i>D2S01</i>	-67.3	59.0	61.9	-75.4
<i>D2S02</i>	-13.9	-17.5	-5.3	-18.0
<i>D2S03</i>	-50.7	-74.3	-75.8	-66.5
<i>D2S04</i>	-7.6	-35.8	-29.0	-5.6
<i>D2S05</i>	169.6	154.9	163.6	103.8
<i>D2S06</i>	-54.1	-71.8	-74.3	-77.8
<i>D2S07</i>	112.9	-97.5	-90.6	94.2
<i>D2S08</i>	7.3	-63.4	-51.0	-87.6
<i>D2S09</i>	151.3	134.1	135.3	121.4

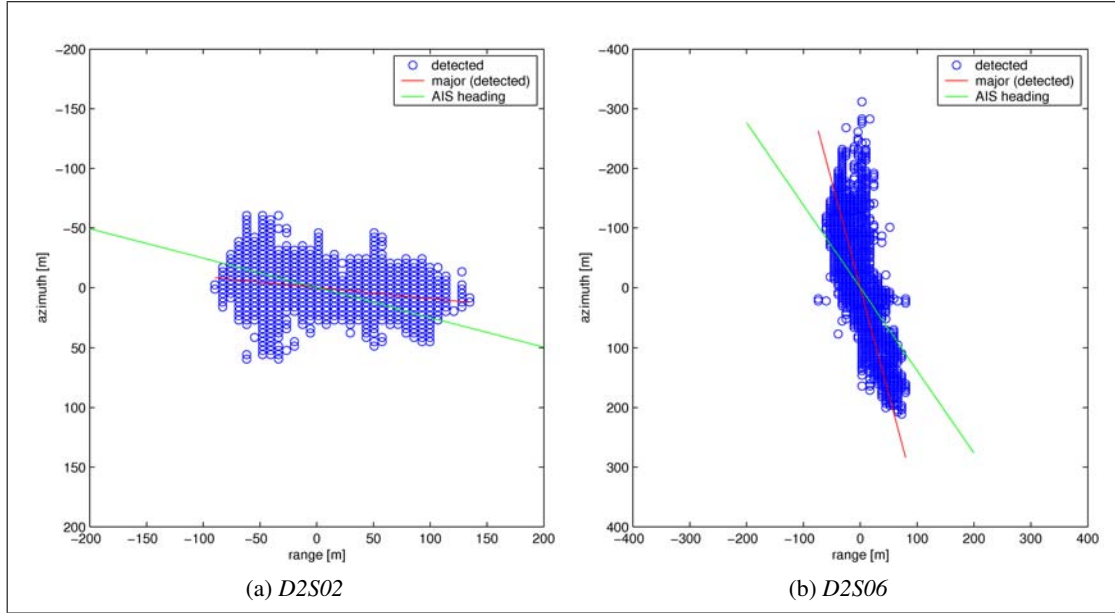


Figure 18: Illustration of detected ship coordinates with the major EV orientation compared to the AIS-derived orientation.

the detected ship pixels, this estimated position was extracted into the matrix \mathbf{P} , similar to \mathbf{D} . The range coordinates in \mathbf{P} and \mathbf{D} are the same, but the azimuth coordinates are not. In \mathbf{P} , they are estimated via the DOA algorithm, while in \mathbf{D} they are the apparent locations as detected in the image. The same EV algorithm was applied to the new set of coordinates, \mathbf{P} , as was applied to \mathbf{D} . The difference is illustrated in Fig. 19 for two ships. In both cases, the aspect angle estimate of the located ship was better than the aspect angle estimate of the detected ship, as shown in Table 5.

However, the estimated position of the ship is not very crisp due to DOA estimation errors, which depend on the SCR. Therefore, the two-channel DOA method, when applied to each pixel in the image domain, does not have a clear advantage over the single channel, image-based method.

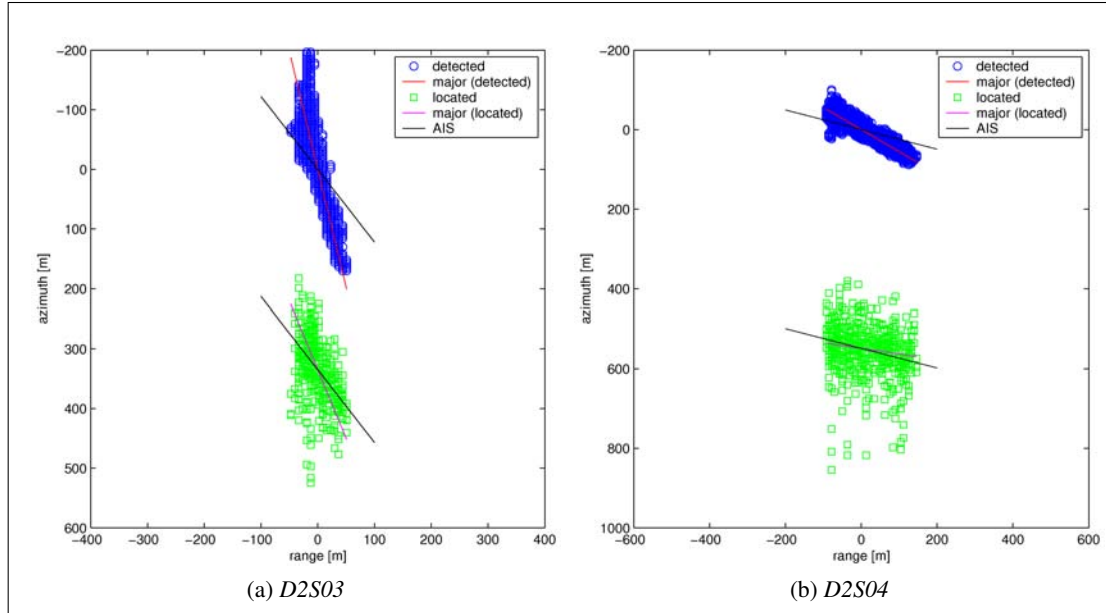


Figure 19: Illustration of detected ship coordinates with the major EV orientation compared to the estimated ship location with its major EV orientation and AIS-derived orientation.

Finally, the images of the two outliers are shown in Fig. 20 and overlaid with the dual-channel processing results. The apparent orientation of *D2S01* is quite different from the DOA result, which is in agreement with the AIS data. *D2S07* is a nominally along-track traveling ship that has a very elongated signature in the SAR image. It is interesting to note that the DPCA technique detected two separate areas of the ship with a gap in between (i.e., no radial motion) and the ATI technique found both positive and negative radial speeds. The DOA algorithm correctly placed the detections within the gap between the two DPCA-detected sections.

We may conclude that the wave field is responsible for most of the estimation problems in the 2009-01-21 data set, but this is not the only source of error.

There is less evidence of wave-induced motion in the 2009-01-19 data set. In this image, all ships were in the Strait of Gibraltar, while the ships from 2009-01-21 were mostly in the Atlantic ocean. Almost all ships in the 2009-01-19 scene were range traveling. The accuracy of the aspect angle estimation for these ships is summarized in Fig. 21 for the EV algorithm. In this case, there are also three outliers, all passenger crafts. Two of them are very fast small catamarans, *D1S01* and *D1S09*, traveling in opposite directions, and the third is the passenger ship *D1S07*. Their signatures do not have the expected shape in the image domain.

Several estimation problems, caused by imaging artefacts, are illustrated below. In most cases, there is a smear in the azimuth direction. Cargo ship *D2S08* from 2009-01-21, passenger ship *D1S07*

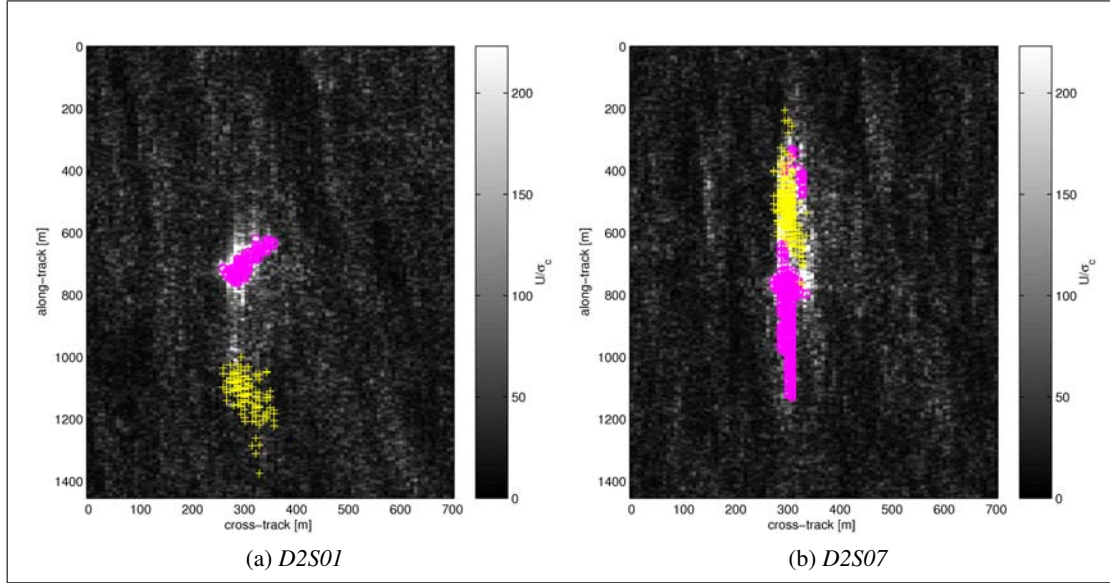


Figure 20: Illustration of ship imaging in a wave field with highlighted pixels detected by the DPCA algorithm and overlaid DOA-estimated positions.

from 2009-01-19, and small passenger catamarans *D1S01* and *D1S09* from 2009-01-19, are such examples. It is difficult to speculate on the source of these effects. For example, the power profile of *D2S08* demonstrates a sudden strong return (Fig. 22) that could have been caused by a rotating reflective surface on the vessel. For *D1S07*, a similar power peak coincides with a brief disruption in the Doppler history (Fig. 23), which supports the same assumption. Such unusual flashes within the vessel signature would cause a smear in the image domain. Images of *D2S08* and *D1S07* are shown in Fig. 22 and 23. Images of the two fast crafts are shown in Fig. 24. All algorithms for aspect angle estimation failed for these ships. Although small, the cargo vessel *D1S12* (Fig. 25 (a)), does not have the same problem as the two fast crafts. The region growing algorithm failed in the case of *D1S06* from 2009-01-19 because it stopped prematurely due to a discontinuity in the ship's signature (Fig. 25 (b)). The EV method worked well in this case.

In the 2009-03-10 scene, aspect angle estimation was mostly good, as shown in Table 6 and Fig. 26. Both the region growing algorithm and the EV algorithm performed well.

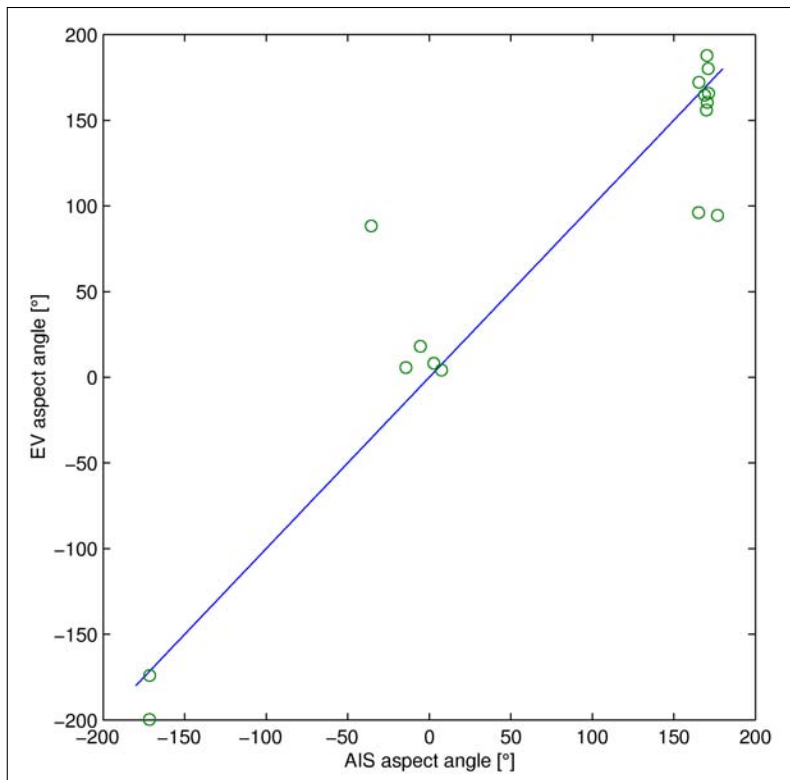


Figure 21: Aspect angle scatter plot for the validated ships on 2009-01-19.

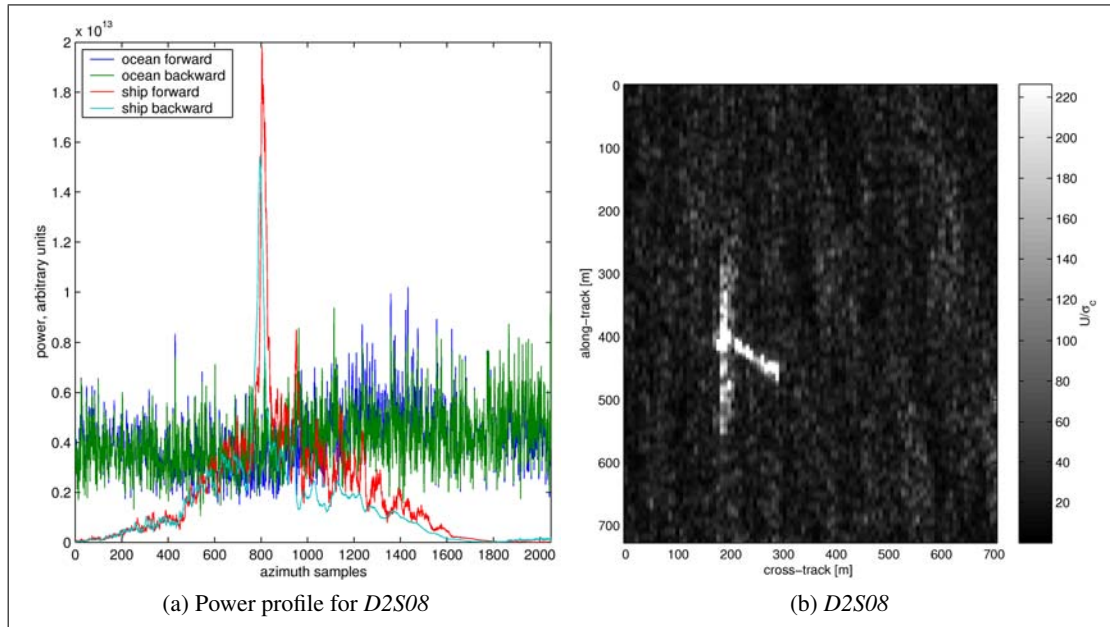


Figure 22: A short strong reflection from *D2S08* may have caused the smear in the azimuth direction.

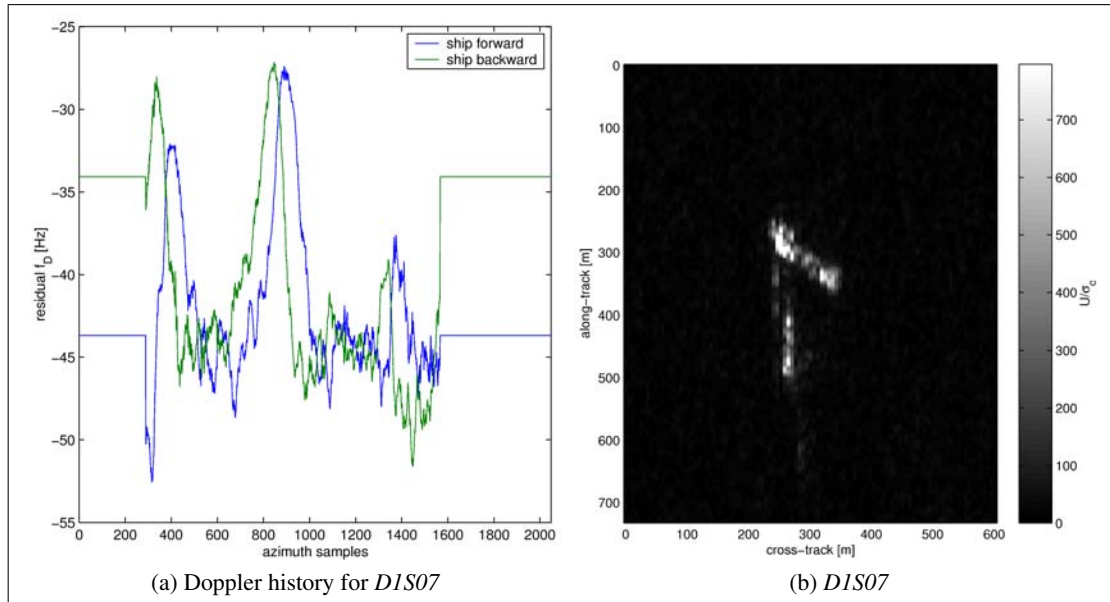


Figure 23: A brief disruption in the Doppler history of *DIS07* may be due to the interference from a moving reflector on the ship, which produced the azimuth smear causing problems in aspect angle estimation.

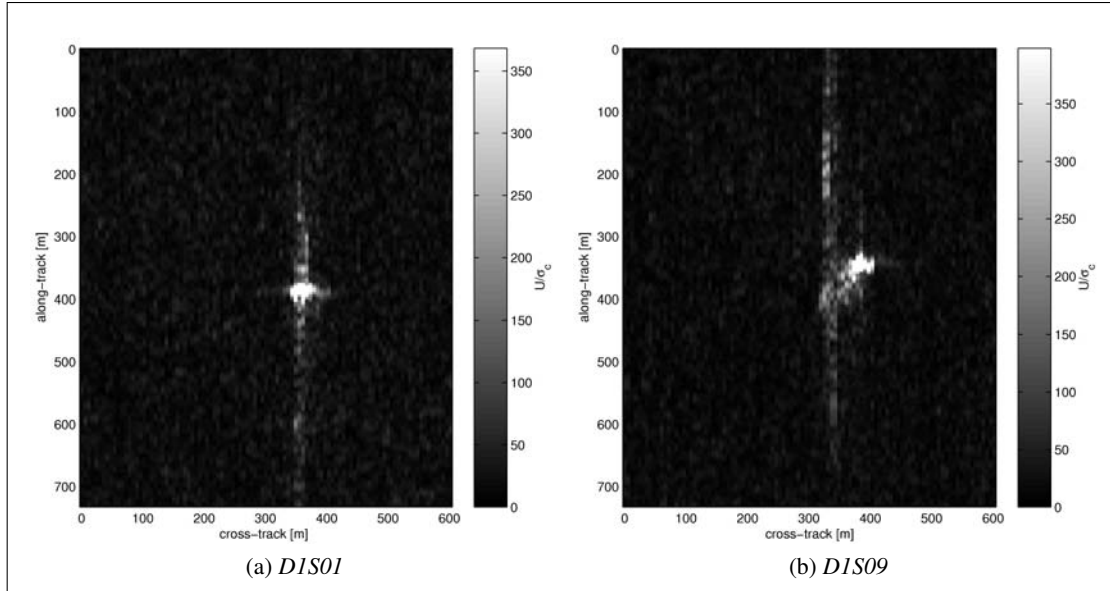


Figure 24: Examples of small and fast crafts that cause problems in aspect angle estimation.

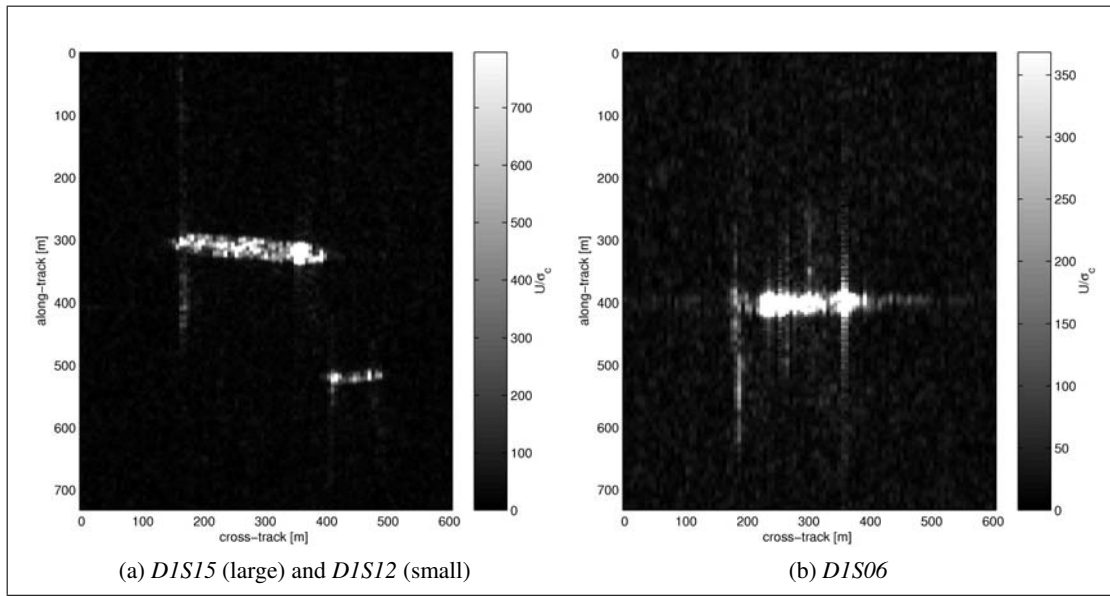


Figure 25: Examples of ships with good aspect angle estimates.

Table 6: Aspect angles estimated on 2009-03-10.

ship	AIS [°]	algorithm	
		region growing [°]	EV detected [°]
<i>D3S01</i>	-8.8	28.4	6.1
<i>D3S02</i>	169.5	161.9	169.4
<i>D3S03</i>	169.5	146.4	128.9
<i>D3S04</i>	-8.6	-21.8	-10.3
<i>D3S05</i>	132.8	132.9	127.6
<i>D3S06</i>	173.7	159.7	166.9
<i>D3S07</i>	-8.2	-19.4	-12.2
<i>D3S08</i>	171.0	170.0	173.3
<i>D3S09</i>	170.5	154.4	164.3

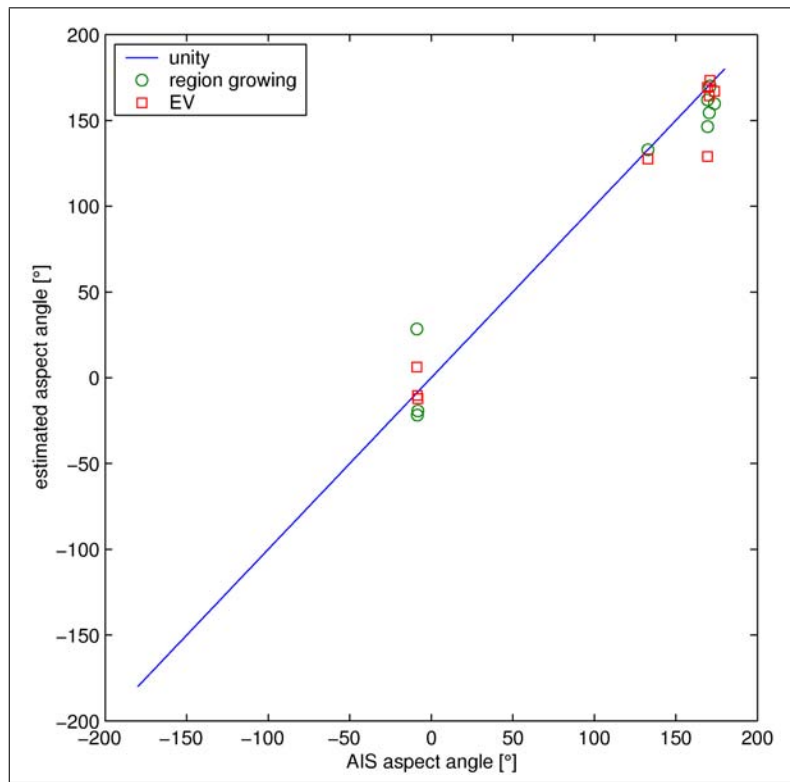


Figure 26: Aspect angle scatter plot for the validated ships on 2009-03-10.

4.3 Experiments with SLC products

Azimuth focusing influences ship signatures in the following ways:

1. The Doppler spectrum is usually not fully preserved, especially if spectral windowing is applied. Since the Doppler spectrum of a ship with non-zero radial speed has a frequency offset relative to the stationary world Doppler spectrum, spectral shaping is non-symmetric for the ship. A portion of the ship's Doppler spectrum may be cut off. This would adversely affect the Doppler offset algorithm.
2. Range cell migration correction (RCMC) that is appropriate for the stationary world is not necessarily suitable for moving targets. In fact, the only difference is in the positioning of the RCMC discontinuity in the Doppler frequency domain. If the process bandwidth is wide (equal or close to PRF), a portion of the ship's signature may receive an inadequate RCMC.
3. CDC calibration may be biased if the Doppler spectrum is shaped according to the internal estimates of the SAR processor. Even if very accurate estimation algorithms are used in the SAR processor, there can be a bias due to the surface motion.

However, if the PRF is high and the processed Doppler bandwidth is large and well preserved (i.e., a boxcar window), the SLC products may be a good starting point for analysing slow moving vehicles such as ships. This may even be a more convenient input since RCMC would not be needed, contrary to the PHP-based analysis.

A simple experiment was devised to test these ideas. The PHP data were first focused using the Range-Doppler algorithm and then were unfocused. The applied Range-Doppler focusing algorithm included all standard steps and the processed bandwidth was varied from full PRF to 70% of the PRF. For spectral shaping, CHASP uses the Kaiser-Bessel window function with the configurable shape factor β . Two values were used, $\beta = 0$ (boxcar window) and $\beta = 2.8$. Unfocusing was implemented as a 1D operation in the Doppler frequency domain so that the RCMC operation was not undone. The main effect of the applied procedure is the controlled reduction of the Doppler bandwidth and the implementation of the RCMC, based on the stationary-world DC.

Reduction of the processed Doppler BW is very noticeable in the power envelope of the adaptive filter used in the Doppler offset algorithm. Fig. 27 (a) represents the most drastic case where only 70% of the PRF is processed in the case of the fastest ship from the 2009-01-19 data set. For better clarity of the plot, only the forward tracking results are shown. Fig. 27 (b) shows the case of a moderately fast ship with processed BW equal to 90% of the PRF. Only backward tracking results are shown in this plot. In comparison with the power profiles from the PHP data, the SLC signatures of these two ships are truncated in slow time. Although this truncation is much less for D2S02, it introduces a significant bias in the estimate of the acquisition time, which causes a bias in the Doppler offset estimate. In all cases, there was a degradation in the accuracy of the radial speed estimates. Two typical plots are shown in Fig. 28 for a relatively slow ship and for a moderately fast one. As expected, high-BW SLC products appear to be acceptable, especially for slower ships. Radial speed estimation using SLC products was biased for most cases. Therefore, various SLC products were compared using the root-mean-square error (rmse) of the estimates as a better metric than the standard deviation. Tables 7 and 8 present the rmse of the radial speed estimates when the

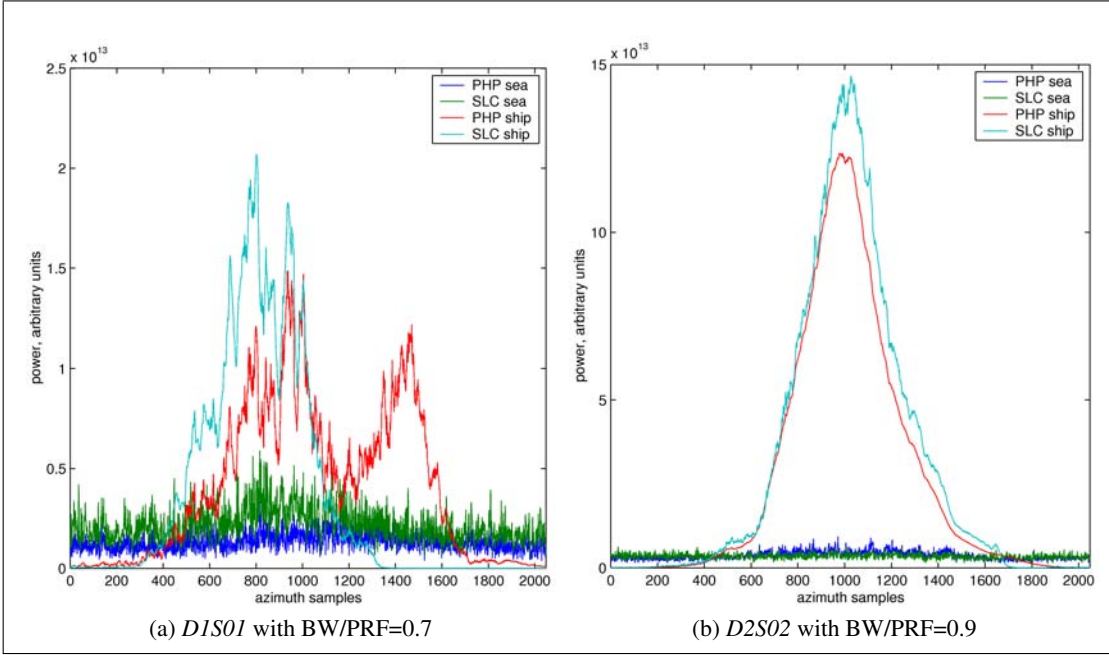


Figure 27: Examples of power profiles extracted from PHP and SLC products for two ships.

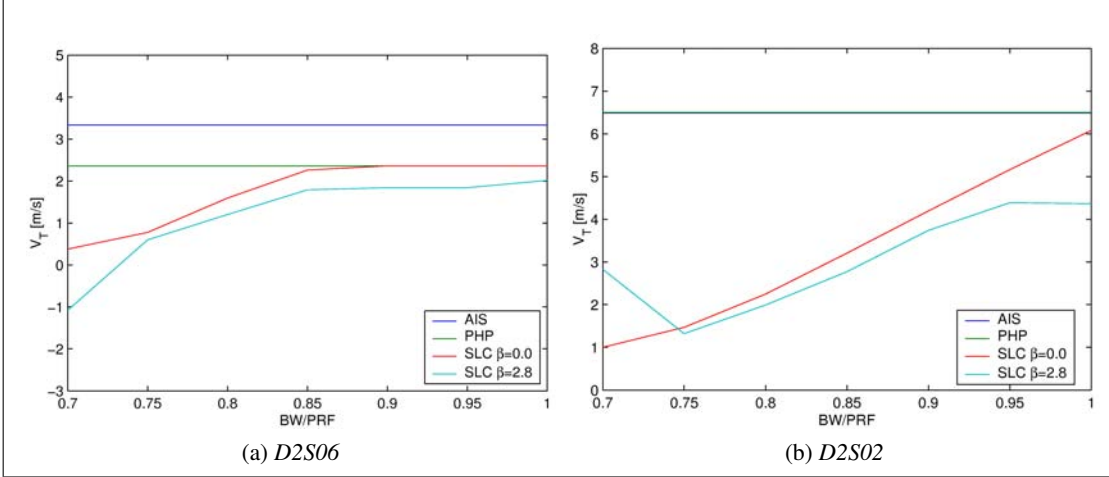


Figure 28: Examples of accuracy degradation with reduced Doppler bandwidth.

processed Doppler BW is reduced. Comparing the two HH scenes, the results are worse for the 2009-01-19 scene because there are two fast crafts present. For the VV scene, the rmse is larger, but for the SLC products with a high BW (over 90% of the PRF) and $\beta = 0$, the rmse is comparable to the rmse for the PHP. If processed BW is less than shown in the table, then the algorithm fails for many ships. As expected, spectral shaping with $\beta > 0$ leads to increased estimation errors.

Table 7: Radial speed rmse for all ships in the SLC products with $\beta = 0$.

BW/PRF	PHP	SLC $\beta = 0$			
	1.00	1.00	0.95	0.90	0.85
2009-01-19 rmse [m/s]	0.8434	1.2023	2.5266	3.6726	4.4881
2009-01-21 rmse [m/s]	0.8968	0.9543	1.0037	1.2227	1.4976
2009-03-10 rmse [m/s]	1.3058	1.5816	1.6132	1.7525	2.4524

Table 8: Radial speed rmse for all ships in the SLC products with $\beta = 2.8$.

BW/PRF	PHP	SLC $\beta = 2.8$		
	1.00	1.00	0.95	0.90
2009-01-19 rmse [m/s]	0.8434	3.3097	3.8827	4.1856
2009-01-21 rmse [m/s]	0.8968	3.9757	3.9922	4.0031
2009-03-10 rmse [m/s]	1.3058	2.4433	2.5644	2.8767

5 Conclusion

Based upon the analysis of 35 known ships within three RADARSAT-2 scenes acquired in MODEX mode and converted to PHP, the following conclusions and observations are offered:

- Adaptive algorithms developed for RADARSAT-1 are applicable to RADARSAT-2, at least when using modes with similar resolution;
- The accuracy of radial speed estimates is similar to that obtained with RADARSAT-1 at similar resolution;
- For HH scenes, the standard deviation of the radial speed estimates was 0.85 m/s, compared to a standard deviation of 0.3 m/s achieved by ATI in the special MODEX mode;
- The adaptive algorithm worked for the VV scene without any modification, albeit with a larger root-mean-square error of 1.3 m/s, compared to a standard deviation of 0.6 m/s achieved by the AT algorithm;
- PHP is the most suitable input for radial speed estimation by adaptive analysis, but a customized SLC product is a reasonable alternative;
- If SLC is used as the input, it is important to ensure a high enough PRF and to process practically the full PRF bandwidth with a box-car shaped spectral window;
- For the first time, VV and HH results are compared for ship radial speed estimation; HH polarization provided a higher accuracy (in the absence of ship wake analysis);
- The importance of a calibrated physical model is affirmed for radial speed estimation;
- Based on the limited data set available in this analysis, the DC and attitude properties of RADARSAT-2 seem to be stable and predictable from the auxiliary data, which may extend the applicability of the physical model to ocean areas without nearby land available for calibration;
- A new approach to ship aspect angle estimation based on eigen analysis was used in the image domain;
- The effect of wave-induced motion on the apparent ship aspect angle is clearly demonstrated, but cannot be resolved in a single aperture SAR image (if no wakes are visible);
- Certain image artefacts can confuse the present algorithm for aspect angle estimation, although this problem can be corrected by visual inspection, which suggests that the algorithm could be further improved.

In an operational setting, it is expected that SAR-derived ship signatures will be fused with AIS data. Any left over ship signatures become ships of interest since they are either non-compliant or non-cooperative with respect to AIS deployment. It is pointed out that these ships are of greatest interest, but have the least known about them. As such, additional processing of the SAR data to derive additional ship information would be beneficial. For example, single-beam ship velocity

estimation algorithms such as those described in this document would be useful to better forecast the future location of the ships of interest if deploying other surveillance assets.

References

- [1] Vachon, P.W. and Dragošević, M.V. (2006), COASP and CHASP processors for strip-map and moving target adaptive processing of EC CV-580 Synthetic Aperture Radar data – Algorithms and software description, (DRDC Ottawa TM 2008-066) Defence R&D Canada – Ottawa.
- [2] Vachon, P.W. and Dragošević, M.V. (2007), Adaptive processing of RADARSAT-1 fine mode data – Ship parameter estimation, (DRDC Ottawa TM 2007-053) Defence R&D Canada – Ottawa.
- [3] Dragošević, M.V. and Vachon, P.W. (2008), Estimation of Ship Radial Speed by Adaptive Processing of RADARSAT-1 Fine Mode Data, *IEEE Geosci. Remote Sens. Lett.*, 5(4), 678–682.
- [4] Goldstein, R.M. and Zebker, H.A. (1987), Interferometric radar map of ocean surface currents, *Nature*, 328, 707–709.
- [5] Chiu, S. (2007), Performance comparison of RADARSAT-2 advanced moving object detection modes, (DRDC Ottawa TM 2007-320) Defence R&D Canada – Ottawa.
- [6] Livingstone, C. and Thompson, A. (2004), The moving object detection experiment on RADARSAT-2, *Can. J. Remote Sens.*, 30(3), 355–368.
- [7] MDA (2002), RADARSAT-2 reference frames and attitude parameters, RSATMDA-148, 1/0 ed, MDA Corporation, 13800 Commerce Parkway, Richmond, B.C., V6V 2J3.
- [8] Lee, T., Leitch, R., Ali, Z., Kroupnik, G., and Raimondo, G. (2004), RADARSAT-2 spacecraft bus design and performance, *Can. J. Remote Sens.*, 30(3), 265–281.
- [9] Ouchi, K., Iehara, M., Morimura, K., Kumano, S., and Takami, I. (2002), Nonuniform azimuth image shift observed in the Radarsat images of ships in motion, *IEEE Trans. Geosci. and Remote Sens.*, 40(10), 2188–2195.
- [10] Dragošević, M.V., Henschel, M.D., and Livingstone, C.E. (2008), An approach to ship motion estimation with dual-receive antenna SAR, In *Proc. of IEEE Radar Conf.*, Rome, Italy.

This page intentionally left blank.

Annex A: Updated CHASP configuration

The CHASP configuration file is documented in [1], which was written in 2006. Since that time, CHASP has evolved. New functionality was added, which is reflected in the configuration file. The current list of controls that can be set via the configuration file is described in full for completeness. All keywords and field values are in ASCII form. Field values represent inputs that are internally interpreted as one of:

- character strings (e.g., file names);
- numbers (i.e., integer or floating point);
- flags or logical values (e.g., Yes, No)

Some fields are required (mandatory), some are optional and some are conditional, as indicated in the following list.

`input_data_file` (**character string**) provides the name of the input file or files with range-compressed data. This entry is mandatory; CHASP will fail without it. For single channel data, the full file name (and path, if different from the current directory) must be provided. It can be any string and may have an arbitrary extension. For two channel or four channel data, only the root part of the file name is required. The completion of the input file names is automatic, according to CHASP conventions. For quad-channel data, the completions are: `hh.rc`, `hv.rc`, `vv.rc` and `vh.rc`. For dual-channel data, the completions are: `fore.rc` and `aft.rc`.

`prf_file` (**character string**) optionally provides the name of the input file with SVs. If present, this file must be in Matlab-4 format and must contain the SAR positions in the ECEF system at the rate of the SAR PRF, starting from the first signal pulse (not necessarily the first range compressed pulse). Georeferencing is not possible if this file is not present. This file may also contain the “PRF/V” values at the same sampling rate.

`channels` (**integer 1, 2 or 4**) tells CHASP how many channels there are in the data set. The default value is 1. For more than one channel, the naming conventions apply.

`first_line` (**integer**) tells CHASP at which input range line to start processing, counting from the beginning of the input range compressed file (which may differ from the start pulse of the signal data). The default is from start of file.

`last_line` (**integer**) tells CHASP where to stop processing, but in most cases it has no effect. Since CHASP processes one and only one block of data, it is actually the block size that determines the last processed line.

`first_sample` (**integer**) tells CHASP at which range sample to start processing, counting from the first sample of the range-compressed data (which may differ from the start sample of the signal data). The default is from start of the range-compressed lines.

`last_sample` (**integer**) tells CHASP what the last sample is for processing. The default is to ingest and process to the end of range compressed lines.

azimuth_focus (**flag** Yes or No) controls whether to perform azimuth compression or not. By default, azimuth compression is not applied.

ZD_frame (**flag** Yes or No) is used conditionally to choose between the zero-Doppler and beam-centre frame if azimuth compression is enabled. It has no effect if azimuth compression is disabled. By default, data are compressed to the zero-Doppler image frame. For No, they are processed to the beam-centre image frame.

RangeDoppler (**flag** Yes or No) is used conditionally to specify which focusing algorithm to use if azimuth compression is enabled. If not selected, the Range-Doppler algorithm is not used by default. Other possibilities include the SPECAN algorithm and the rudimentary 1D “matched filter” algorithm (inherited from an earlier airborne SAR processor, which can tolerate only small unambiguous DC offsets and has no capability for RCMC in frequency domain).

specan (**flag** Yes or No) is used conditionally to specify which focusing algorithm to use if azimuth compression is enabled. If not selected, the SPECAN algorithm is not used by default. Other possibilities include the Range-Doppler algorithm and the rudimentary 1D “matched filter” algorithm.

azimuth_align (**flag** Yes or No) is used conditionally to specify if any azimuth shift should be performed when the number of channels is more than one. This option can be used for azimuth co-registration. If alignment is desired, it is done by interpolating the data of certain channels. For quad-channel data, it is usually the VV and VH channels that have to be interpolated to match the acquisition times of the HH and HV data. For dual-channel data, the aft channel might be shifted in slow time. The default is not to do any azimuth shifting. If enabled, the amount of shifting is defined in other fields.

azimuth_shift_hh (**floating point number**)

azimuth_shift_hv (**floating point number**)

azimuth_shift_vv (**floating point number**)

azimuth_shift_vh (**floating point number**) defines the amount of azimuth shift for different channels and are applied if azimuth (slow time) shifting is enabled. They are specified in terms of the pulse spacing. For quad-channel data, each value is applied to the named polarization. For dual channel data, the hv value is applied to the aft channel. These values have no effect on the single channel data. The default values are 0.

compensate_radial (**flag** Yes or No) tells CHASP if any range shifting is required for certain channels. This option can be used for range co-registration, i.e., if it is necessary to align delays for different channels and if relative delays are not corrected in pre-processing. The default is not to do any range shifting. If enabled, the amount of range or fast time shifting is defined in other fields.

range_shift_hh (**floating point number**)

range_shift_hv (**floating point number**)

range_shift_vv (**floating point number**)

`range_shift_vh (floating point number)` defines the amount of range shift for different channels and are applied if range (fast time) shifting is enabled. They are specified in terms of the range spacing. For quad-channel data, each value is applied to the named polarization. For dual channel data, the `hh` value is applied to the fore channel and the `hv` value is applied to the aft channel. For single channel data, the `hh` value is applied. The default values are 0.

`rcmc (flag Yes or No)` is used to indicate if RCMC in Doppler domain should be done or not. RCMC is always included in the Range-Doppler algorithm, but it may be desired even if data are not focused.

`doppler_looks (integer 1 or 2)` defines how many Doppler looks to produce in the case that azimuth focusing is enabled. The default value is 1. There are other fields that define what to do with looks if two of them are created.

`window_shape (floating point number)` defines the shape of the Kaiser-Bessel window if filters are applied in either range or azimuth. The default value is 0.0, which means a box-car window.

`full_bandwidth (floating point number)` specifies the available DBW normalized by the PRF if azimuth filtering (focusing or shifting) is applied. If focusing is enabled, this field must be defined.

`look_bandwidth (floating point number)` specifies the processed DBW per look normalized by the PRF if azimuth filtering (focusing or shifting) is applied. If focusing is enabled, this field must be defined and not be larger than the full bandwidth.

`look_offset (floating point number)` tells CHASP how to position Doppler looks relative to the DC and is expressed in fractions of the PRF. The default value is 0. For non-zero values, the created Doppler look or looks would not be symmetric about the DC.

`look_overlap (floating point number)` specifies the amount of overlap between looks as a fraction of the PRF. It is applicable only if two looks are created.

`coherence (flag Yes or No)` tells CHASP if coherence between azimuth looks should be computed. This option makes sense only under certain settings that are explained in detail in [1] (when two complex azimuth looks are being created and azimuth resizing is enabled). The default value is `No`.

`mag_coherence (flag Yes or No)` is used conditionally to choose between different ways to compute coherence. The default value is `No`, which means that coherence is measured on complex looks, while `Yes` tells CHASP to measure coherence on the magnitude of the azimuth looks.

`norm_coherence (flag Yes or No)` is used conditionally to choose between different ways to compute coherence. By definition, coherence is a normalized value, but this is not the default in CHASP. The default is `No`, which produces a spatially smoothed interferogram between azimuth looks.

`multi_look (flag Yes or No)` controls whether processed data should be converted to magnitude, thus losing the phase information. The default is to leave data as complex values. This flag controls single look and two look data, focused or not.

`spatial_size` (**flag** Yes or No) tells CHASP whether resampling in azimuth is needed to produce square pixels of ground coverage. There is no provision to control the square pixel size. The data can only be resampled with smoothing in azimuth to match the spacing in ground range. The same operation is used in the evaluation of inter-look coherence.

`correlate_looks_len` (**integer**) is used conditionally to specify the length of the cross-correlation in the azimuth direction between Doppler looks. It is used only if two looks are created and converted to magnitude. Its purpose is to estimate target misregistration in the two looks. The default value is 0 (not applied).

`auto_fit` (**flag** Yes or No) is used to enable polynomial fitting of the Doppler phase modulation revealed by measuring look-to-look misregistration (as part of the “map-drift” algorithm). The default value is No. This feature can be used only iteratively, i.e., CHASP has to run multiple times with positive `correlate_looks_len` and it can perform adaptive fitting in the subsequent run.

`range_look` (**flag** No or Up or Low) provides the option of creating a specified range look. The default option is No, which leaves the range spectrum unchanged. The other two options are used to extract the upper or the lower band from the full range BW (i.e., pulse BW).

`range_bb` (**flag** Yes or No) is used conditionally to reposition (in frequency) the selected range look to the base band. This is a step in range multi-looking and, also, a step in some algorithms for PRF ambiguity resolution. However, CHASP does not have full capabilities for such algorithms (they would have to be completed externally).

`chirp_bw` (**floating point number**) defines the pulse BW normalized by the sampling frequency and serves for extraction of the range looks, if required. Otherwise, it has no effect.

`doppler_grid_rg` (**integer**) sets the number of grid elements in the range direction for calculating the DC estimates. DC estimation is disabled if this number is 0, which is the default.

`geoid_over_ellipsoid` (**floating point number**) is used to specify the terrain elevation over the reference Global Ellipsoid (WGS84). It is used for the purpose of georeferencing, if applied. The default value is 0.0.

`spread_loss` (**integer**) is the degree of the power spread loss function to be applied in range. The default is 0, which makes no radiometric changes to the data. A positive number can be used to correct possible deficiencies of the radiometric normalization applied in the pre-processing.

`reference_range` (**floating point number**) is used as a reference to normalize the slant range before evaluating the spread loss radiometric correction, if required.

`Pauli` (**flag** Yes or No) tells CHASP if the conversion to the Pauli polarimetric basis should take place. This option is valid only for quad-channel data on condition that all four channels are processed concurrently, i.e., loaded together into CHASP’s memory space. The default value is No.

`DPCA` (**flag** Yes or No) is used to find the channel difference, sample by sample. This option is valid only for dual channel data on condition that both channels are processed concurrently, i.e.,

loaded together into CHASP’s memory space. The default value is `No`. This flag controls only the subtraction function and no other step of the standard DPCA technique, which is controlled via other settings (e.g., channel co-registration and balancing). Therefore, this flag can be useful for other operations such as beamforming.

`ATI` (**flag** `Yes` or `No`) is used to find the channel interferogram, sample by sample. This option is valid only for dual channel data on condition that both channels are processed concurrently, i.e., loaded together into CHASP’s memory space. The default value is `No`. This flag controls only the complex conjugate multiplication function and no other step of the standard ATI technique, which is controlled via other settings (e.g., channel co-registration and balancing). Therefore, this flag can be useful for other operations such as the DOA algorithm.

`DOA` (**flag** `Yes` or `No`) is used to enable the essential step of the implemented DOA algorithm and that is the multiplication of the aft channel with a ramp phase function in slow time. This option is valid only for dual channel data on condition that both channels are processed concurrently, i.e., loaded together into CHASP’s memory space and the effective ATI baseline must be defined. The default value is `No`. This flag is responsible only for the de-ramping step of the DOA algorithm (ATI flag must be set to complete the algorithm). If applicable, there are separate optional fields to specify the reference point for de-ramping.

`ADI` (**flag** `Yes` or `No`) is used to enable the essential step of the “azimuth displacement indicator”, an algorithm that achieves the same functionality as the standard ATI algorithm. This option is valid only for dual channel data on condition that both channels are processed concurrently, i.e., loaded together into CHASP’s memory space and the effective ATI baseline must be defined. The default value is `No`. This flag is responsible only for the multiplication of the aft channel with a ramp phase function before and after azimuth focusing (ATI and `azimuth_focus` flags must be set to complete the algorithm). If applicable, there are separate optional fields to specify the reference point for de-ramping.

`balance_dPCA` (**flag** `Yes` or `No`) is used to enable channel balancing. This option is valid only for dual channel data on condition that both channels are processed concurrently, i.e., loaded together into CHASP’s memory space. The default value is `No`. If this flag is set, channel imbalance is evaluated (including the ratio of the average magnitude and the average of the phase difference) and is compensated by multiplication of the aft channel with a complex scalar. However, the estimated imbalance may be overwritten by external values.

`balance_ratio` (**floating point number**) sets an external value to overwrite CHASP’s internal measurement of the channel magnitude imbalance. The corresponding compensation is applied to dual channel data if this value is positive and if channel balancing is enabled.

`balance_rad` (**floating point number**) sets an external value to overwrite CHASP’s internal measurement of the channel phase imbalance. This value is given in radians. The corresponding compensation is applied to dual channel data if `balance_ratio` has a positive value and if channel balancing is enabled. The default value is 0.0. An external value can be used if any linear combination of two channels is desired, e.g., for beamforming.

`auto_focus` (**flag** `Yes` or `No`) is used to enable the Doppler frequency tracking algorithm. Additional parameters related to this algorithm can be set through other fields. The default value

is No. This algorithm cannot run together with azimuth focusing. If tracking is enabled, focusing is disabled automatically.

`alpha` (**floating point number**) is a design parameter for the Doppler tracking algorithm used if `auto_focus` is enabled. It controls the initial notch width of the adaptive filter. The recommended value is 0.8, which is also the default.

`track_range` (**integer**) is optionally used to indicate the range bin at which the target of interest is located. If provided, this input is used by the tracking algorithm and for extracting various target features on condition that such algorithms are enabled. This parameter is not necessarily used in a strict way since the corresponding CHASP algorithms may search for the brightest point in the neighbourhood of the given range bin. If not provided, these algorithms will pick the brightest focused point.

`track_azim` (**integer**) is optionally used to indicate the azimuth bin at which the target of interest is located. If provided, this input is used by the tracking algorithm and for extracting various target features on condition that such algorithms are enabled. This parameter is not necessarily used in a strict way since the corresponding CHASP algorithms may search for the brightest point in the neighbourhood of the given azimuth bin. If not provided, these algorithms will pick the brightest focused point.

`bunch_r` (**integer**) is optionally used to indicate the number of range bins occupied by the target of interest. If provided, this input is used by the tracking algorithm and for extracting various target features. If not provided, a suitable value is found automatically by the corresponding CHASP algorithms.

`bunch_a` (**integer**) is optionally used to indicate the number of azimuth bins occupied by the target of interest. If provided, this input is used by the tracking algorithm and for extracting various target features. If not provided, a suitable value is found automatically by the corresponding CHASP algorithms.

`track_strict` (**flag Yes or No**) is used to enforce the use of `track_range` and `track_azim` in a strict way, i.e., without any adjustments that CHASP algorithms would otherwise apply. The default value is No.

`phase_order` (**integer 0 to 4**) defines the polynomial order used to fit the phase modulation revealed by Doppler tracking or by iterative use of look correlation.

`auto_correct` (**flag Yes or No**) is used to enable adaptive phase compensation in slow time domain using the estimation results from previous CHASP runs. The default value is No. If enabled, this feature uses either a polynomial phase compensation (if `phase_order` is positive) or a non-parametric phase compensation extracted previously by the tracking algorithm and smoothed.

`smooth` (**integer**) defines the size of the weighted moving average filter applied to smoothen the tracking results if `auto_correct` is applied. This value is used both for the extracted Doppler phase variations and for the extracted range variations of the tracked target over slow time. The recommended value is 20, which is also the default.

ACHIRP (**flag** Yes or No) plays a similar role as `auto_correct`, but applies a second order phase compensation defined by the along-track speed, which is set in a separate field.

`range_migration` (**flag** Yes or No) is used to enable RCMC in the time domain. The default value is No. This option is typically, but not automatically, selected if tracking or SPECAN algorithms are used. If applicable, there are separate optional fields to specify the reference point for RCMC in the time domain.

`adaptive_migration` (**flag** Yes or No) is used to enable adaptive RCMC in the time domain. The default value is No. This feature can be used only iteratively, i.e., CHASP has to run once with `auto_focus` enabled and can apply adaptive RCMC in the next run.

`skew_azim` (**integer**) is used conditionally to specify the reference pulse position for RCMC in time domain, DOA or ADI de-ramping. The default value is the centre of the processing block.

`locate` (**flag** Yes or No) is used to request calculation of the target radar cross section (RCS) and clutter σ^0 and, possibly, other target attributes. The default value is No. If data are converted to magnitude (`multi_look` option turned on), this flag enables the region growing algorithm, which estimates the extent and orientation of the target. Other attributes include the slant range, time, ambiguity distance in range and azimuth and an estimate of the ambiguity-to-target ratio. If the “prf” file is provided, incidence angle and geographic coordinates of the target are calculated, as well. By default, the target is defined as the brightest spot in the image with its immediate surrounding (as determined by the region growing algorithm). However, if `track_range` and `track_azim`, `bunch_r` and `bunch_a` entries are provided, they limit the area in which CHASP searches for a maximum, while `track_strict` prevents any search and enforces the external definition of the target.

`measure_contrast` (**flag** Yes or No) is used to request the evaluation of contrast in the area around the target. The default value is No. This feature can be used only if `locate` is enabled. The area in which contrast is measured is automatically defined based on the target bounds as estimated by the region growing algorithm, but it can also be set to a desired value via separate optional fields.

`window_range` (**integer**) is optionally used to indicate the number of range bins, centred at the target position, where contrast must be measured if `measure_contrast` is enabled. If omitted, an adaptive window is used based on the region growing algorithm.

`window_azimuth` (**integer**) is optionally used to indicate the number of azimuth bins, centred at the target position, where contrast must be measured if `measure_contrast` is enabled. If omitted, an adaptive window is used based on the region growing algorithm.

`profile` (**flag** Yes or No) is used to request the evaluation of the power profile along azimuth by averaging in range. The result is expressed in the dB scale. The number of averaged range bins depends on the range extent of the target (as estimated or set externally) and on the range displacement of the ambiguities. This feature can be used for plotting and visualizing the ambiguities. The default value is No.

`pgm_out` (**flag** Yes or No) is used to create a PGM file as CHASP output. The default value is No. This option is valid if `multi_look` is on.

`ppm_out` (**flag** Yes, No **or** Pauli) is used to create a PPM file as CHASP output where channels are colour coded. The default value is No. This option is valid only for quad-channel data if `multi_look` is on. The Pauli option is allowed only if all channels are processed concurrently, i.e., loaded together into the CHASP's memory space.

`pgm_floor` (**floating point number**) is used conditionally to specify the cut-off magnitude in dB (relative to the maximum intensity) if CHASP is doing conversion to an 8-bit output format such as PGM and PPM. This feature is useful for creating a preview of the processed data.

`relative_dc_offset` (**floating point number**) sets the DC value normalized by the PRF that is to be used in many algorithms such as focusing, RCMC or azimuth shifting. The default value is 0.0.

`relative_dc_clutter` (**floating point number**) sets the DC value normalized by the PRF that is representative of the background clutter. This value is not used for processing. It is used as a reference for radial speed estimation based on the difference between the estimated target DC and this clutter value. The default value is 0.0.

`relative_v_offset` (**floating point number**) sets the target along-track speed normalized by the SAR speed. It can be used to modify the Doppler rate for azimuth focusing. Alternatively, it can be used to compensate the effect of the target along-track speed if ACHIRP is used. The default value is 0.0. This feature is often used in iterative CHASP runs, where an estimated value from one run becomes an input parameter for the next.

`prf_over_v` (**floating point number**) is used to optionally enter the focusing parameter f_p/v_{eff} , which is the ratio of the PRF and the effective speed of the SAR platform. This parameter is needed if `azimuth_focus` is enabled. Another possible source of this parameter is the "prf" file, but can be overwritten by this configuration field. If neither source of f_p/v_{eff} is available, CHASP will fail.

`sin_inci_ang` (**floating point number**) is used to optionally enter the sine of the incidence angle, which is needed for some operations (spatial_size or calculation of σ^0). Another possible source of this parameter is the "prf" file, but this is an option to provide the incidence angle (externally calculated) even if the "prf" file is missing.

`wavelength` (**floating point number**) is the only way to define the SAR wavelength for CHASP. It is required for many calculations and most functions will fail if it is not provided.

`range_slant_spacing` (**floating point number**) is the only way to define the slant range sample size for CHASP. It is required for many calculations and most functions will fail if it is not provided.

`azimuth_beamwidth` (**floating point number**) provides the azimuth beam width in degrees, which is used to determine the length of the tracking window when `auto_focus` is enabled. It is required for the tracking algorithm.

`baselineATI` (**floating point number**) provides the effective baseline length that is used if DOA or ADI are enabled. It is not needed otherwise.

`block_lines (integer)` defines the size of the data block in azimuth. Currently, the maximum allowed value is 16 K. In the current implementation, this value does not have to be a power of 2. The default value is 1 K, which is insufficient if CHASP is used for RADARSAT focusing (CHASP would fail).

`processors (integer)` defines the number of parallel processes that will be used to execute CHASP. The default value is 1. Almost all functions can be executed by parallel multiple tasks. Some adaptive functions, namely tracking and region growing, are not designed to be parallelized.

`parts (integer)` defines the number of parts per block of each channel when CHASP does data partitioning. The default value is 1. If the number of parts and the number of processors are both greater than 1, different processors will be in charge of different parts.

`channels_together (integer)` defines the number of channels to be loaded together into CHASP's memory space and processed concurrently. The default value is 1. For single channel data, this number must be 1. For dual channel data, this number can be 1 or 2, but certain functions require the presence of both channels (e.g., DPCA, ATI). For quad-channel data, this number can be 1, 2 or 4, but certain functions require the presence of all channels (Pauli).

`interp_size (integer)` defines the length of the "sinc" interpolation kernel used for resampling. In the current implementation, it must be an odd number. The default value is 5, but the usual value is 11.

`interp_fractions (integer)` defines the granularity of the sub-pixel shifts, i.e., the number of different "sinc" interpolation kernels used for resampling. The default value is 16, but the usual value is 64.

`change_input_endian (flag Yes or No)` is used to request byte swapping at input. The default value is No. This option can be useful when processing data created with a different byte order.

`change_output_endian (flag Yes or No)` is used to request byte swapping at output. The default value is No. This option can be useful when processing data that will be used on some platform with a different byte order.

This page intentionally left blank.

Annex B: Data processing procedure

The Gibraltar scenes were processed systematically using a slightly modified version of the procedure that had been applied earlier to the RADARSAT-1 Dover scenes. The difference is only in the pre-processing and data preparation, while the actual CHASP algorithms are the same.

The processing procedure is as follows:

1. Data preparation, which includes two steps:
 - (a) Preprocessing by MDA's Pre-Processing Module
 - (b) Beamforming using the following CHASP configuration options:

azimuth_focus	No
azimuth_align	No
DPCA	Yes
balance_dpca	Yes
balance_ratio	0.933
balance_rad	2.79159

The entered values are examples. The value for the phase (balance_rad) must be $\pi - \phi_c$ where ϕ_c defines the phase of the steering vector \mathbf{G} defined in Section 2.2. Since the DPCA operation (channel subtraction) is used, the sign must be inverted.
2. Creation of the file with the SVs at the rate of the PRF by:
 - (a) Extracting a SV for a known pulse of the original data
 - (b) Short term orbit propagation by pulse-to-pulse numerical integration using low-order (3) zonal harmonics of the Earth gravitational potential (which could be replaced by an orbital interpolator)
3. Attitude estimation, which includes the following steps:
 - (a) Running CHASP in small overlapping tiles (with tile size of 256 range bins and 2048 azimuth bins and successive steps of 128 bins in range and azimuth) using two iterations for:
 - i. Enabling and executing DC estimation without focusing
 - ii. Extracting preliminary DC estimates from the CHASP header
 - iii. Focusing with the preliminary DC estimates and performing DC estimation after focusing to provide refined DC estimates
 - (b) Appending a land mask flag to the CDC map using georeferencing information for each tile and using a coarse global land-water mask
 - (c) Calculating v_{down} , v_{right} , v_{for} and γ defined in Section 2.1 for each tile
 - (d) Solving (1) in the least squares (LS) sense
4. Information extraction from the AIS data, which includes:
 - (a) Calculating image location from the predicted ship geographical location

- (b) Projecting ship velocity given as speed and heading onto the LOS, cross-track direction and along-track direction

5. Extraction and analysis of each ship signature including:

- (a) Setting start and stop range and azimuth sample for the specific ship signature
- (b) Calculating the nominal DC for the range of interest using the estimated attitude and SVs (applying (1))
- (c) Calculating the focusing parameter f_p/v_{eff} for the range of interest using the SVs (with v_{eff} defined in [3])
- (d) Focusing the chip of interest with the nominal parameters and saving the “before” image
- (e) Running the tracking algorithm iteratively (four times) where each iteration consists of:
 - i. Enabling and executing the tracking algorithm using current processing values
 - ii. Extracting the resulting DC and along-track speed correction from the CHASP header
 - iii. Setting the new DC value and, optionally, the new along-track speed for the next iteration
- (f) Saving the final tracking results (extracted Doppler history and power profiles, speed estimates, fitting results)
- (g) Focusing with the final DC value and, optionally, the along-track speed adjustment and saving the “after” image
- (h) Calculating target attributes, which includes:
 - i. RCS and σ^0 calculation
 - ii. Region growing algorithm
 - iii. Georeferencing
- (i) Performing the map-drift algorithm in steps:
 - i. Zooming on the target (oversampling 4 times in range and 8 times in azimuth) and extracting two Doppler looks
 - ii. Evaluating look cross-correlation and measuring azimuth misregistration
 - iii. Fitting a model to measured azimuth misregistration

6. Collection of estimation results from all ships

List of acronyms

ASCII	American standard code for information interchange
AIS	Automatic identification system
ATI	Along-track interferometry
BW	Bandwidth
CHASP	Chip-based adaptive SAR processor
CDC	Clutter Doppler centroid
COASP	Configurable airborne SAR processor
DC	Doppler centroid
DOA	Direction of arrival
DPCA	Displaced phase center antenna
DRDC	Defence R&D Canada
ECEF	Earth centred, Earth fixed (system)
ECI	Earth centred inertial (system)
EV	Eigen-value
HH	Horizontal transmit, horizontal receive (polarization)
LS	Least squares
LOS	Line of sight
MDA	Mac Donald, Dettwiler and Associates Ltd. (Corporation)
MODEX	Moving object detection experiment
PGM	Portable gray map (format)
PHP	Phase history product
PPM	Portable pixel map (format)
PRF	Pulse repetition frequency
R&D	Research & Development
RCMC	Range cell migration correction
RCS	Radar cross section
RMS	Root-mean-square
rmse	Root-mean-square error
SAR	Synthetic aperture radar
SCR	Signal-to-clutter ratio
SLC	Single look complex
SNR	Signal-to-noise ratio
VV	Vertical transmit, vertical receive (polarization)
WGS84	World geodetic system 1984

This page intentionally left blank.

DOCUMENT CONTROL DATA

(Security classification of title, body of abstract and indexing annotation must be entered when document is classified)

1. ORIGINATOR (The name and address of the organization preparing the document. Organizations for whom the document was prepared, e.g. Centre sponsoring a contractor's report, or tasking agency, are entered in section 8.)			2. SECURITY CLASSIFICATION (Overall security classification of the document including special warning terms if applicable.)		
<p>Defence R&D Canada – Ottawa 3701 Carling Avenue, Ottawa, Ontario, Canada K1A 0Z4</p>			<p>UNCLASSIFIED</p>		
3. TITLE (The complete document title as indicated on the title page. Its classification should be indicated by the appropriate abbreviation (S, C or U) in parentheses after the title.)					
<p>Estimation of ship velocity by adaptive processing of single aperture RADARSAT-2 data</p>					
4. AUTHORS (Last name, followed by initials – ranks, titles, etc. not to be used.)					
<p>Vachon, P.W.; Dragošević, M.V.</p>					
<p>5. DATE OF PUBLICATION (Month and year of publication of document.)</p>		<p>6a. NO. OF PAGES (Total containing information. Include Annexes, Appendices, etc.)</p> <p>66</p>		<p>6b. NO. OF REFS (Total cited in document.)</p> <p>10</p>	
7. DESCRIPTIVE NOTES (The category of the document, e.g. technical report, technical note or memorandum. If appropriate, enter the type of report, e.g. interim, progress, summary, annual or final. Give the inclusive dates when a specific reporting period is covered.)					
<p>Technical Memorandum</p>					
8. SPONSORING ACTIVITY (The name of the department project office or laboratory sponsoring the research and development – include address.)					
<p>Defence R&D Canada – Ottawa 3701 Carling Avenue, Ottawa, Ontario, Canada K1A 0Z4</p>					
<p>9a. PROJECT NO. (The applicable research and development project number under which the document was written. Please specify whether project or grant.)</p> <p>15el04</p>		<p>9b. GRANT OR CONTRACT NO. (If appropriate, the applicable number under which the document was written.)</p>			
<p>10a. ORIGINATOR'S DOCUMENT NUMBER (The official document number by which the document is identified by the originating activity. This number must be unique to this document.)</p> <p>DRDC Ottawa TM 2009-109</p>		<p>10b. OTHER DOCUMENT NO(s). (Any other numbers which may be assigned this document either by the originator or by the sponsor.)</p>			
11. DOCUMENT AVAILABILITY (Any limitations on further dissemination of the document, other than those imposed by security classification.)					
<p>(X) Unlimited distribution <input type="checkbox"/> Defence departments and defence contractors; further distribution only as approved <input type="checkbox"/> Defence departments and Canadian defence contractors; further distribution only as approved <input type="checkbox"/> Government departments and agencies; further distribution only as approved <input type="checkbox"/> Defence departments; further distribution only as approved <input type="checkbox"/> Other (please specify):</p>					
12. DOCUMENT ANNOUNCEMENT (Any limitation to the bibliographic announcement of this document. This will normally correspond to the Document Availability (11). However, where further distribution (beyond the audience specified in (11)) is possible, a wider announcement audience may be selected.)					
<p>Unlimited</p>					

13. ABSTRACT (A brief and factual summary of the document. It may also appear elsewhere in the body of the document itself. It is highly desirable that the abstract of classified documents be unclassified. Each paragraph of the abstract shall begin with an indication of the security classification of the information in the paragraph (unless the document itself is unclassified) represented as (S), (C), (R), or (U). It is not necessary to include here abstracts in both official languages unless the text is bilingual.)

Adaptive processing of RADARSAT-2 synthetic aperture radar (SAR) imagery of known ships acquired near the Strait of Gibraltar provides estimates of the ship radial speed along the radar line of site and the ship aspect angle, which can be combined to provide an estimate of the ship velocity in the absence of a visible ship wake. Using a Doppler offset algorithm, it was found that the standard deviation of the radial speed estimates was 0.85 m/s for 26 ships in two HH scenes, compared to 0.3 m/s using along-track interferometry (ATI) algorithms, and was 1.3 m/s for 9 ships in a VV scene, compared to 0.6 m/s using ATI algorithms. It was shown that ship aspect angle estimation can be complicated by wave-induced ship motion, which can smear or change the orientation of the imaged ship signature. Validation was carried out against coastal-received Automatic Identification System (AIS) data. It is apparent that ship velocity estimation is feasible for single aperture SARs in the absence of a visible ship wake signature, which could be useful for tracking ships that are not transmitting AIS data.

14. KEYWORDS, DESCRIPTORS or IDENTIFIERS (Technically meaningful terms or short phrases that characterize a document and could be helpful in cataloguing the document. They should be selected so that no security classification is required. Identifiers, such as equipment model designation, trade name, military project code name, geographic location may also be included. If possible keywords should be selected from a published thesaurus. e.g. Thesaurus of Engineering and Scientific Terms (TEST) and that thesaurus identified. If it is not possible to select indexing terms which are Unclassified, the classification of each should be indicated as with the title.)

RADARSAT-2
Synthetic aperture radar
SAR
Ship detection
Velocity estimation
SAR processing

Defence R&D Canada

Canada's leader in Defence
and National Security
Science and Technology

R & D pour la défense Canada

Chef de file au Canada en matière
de science et de technologie pour
la défense et la sécurité nationale



www.drdc-rddc.gc.ca